UNIVERSITÀ DEGLI STUDI DI PADOVA

Dipartimento di Fisica e Astronomia “Galileo Galilei”

Master Degree in Physics of Data

Final dissertation

Addressed coherent manipulation of quantum bits encoded in strontium ions

Supervisor	Candidate
Prof. Caterina Braggio	Tommaso Faorlin
Prof. Markus Hennrich	

Academic year 2021/2022

Abstract

In recent times, we have witnessed a very important growth in the field of quantum computing. Efforts on the experimental side are directed towards obtaining a fully functional quantum computer that obeys DiVincenzo's criteria, and the true capabilities of such a machine are not yet fully known. Similar to this machine that can be programmed as wished, a quantum simulator can be initialised to solve a specific problem or a small piece from a greater problem, by evolving and measuring the state of the qubits used. This is the framework in which this thesis project, at the Trapped Ion Quantum Technologies group at Stockholm University, takes place. The work concerns a quantum simulator built on a linear quadrupole trap, which confines $^{88}\mathrm{Sr}^{+}$ ions in a well-defined region of space. The goal is to simulate, using Zemax OpticStudio, and build an optical setup capable of addressing single ions with the 674 nm laser, and performing single-qubit, multi-qubit and entangling operations on a few-qubit ion string.

Contents

List of Figures

List of Tables

Introduction

Most of the physical laws we use to describe the behaviour of slow and heavy objects in everyday life lose their validity when applied to atomic-scale objects. So far, the most accurate description of phenomena, such as the fact that the electron does not have a well-defined position in space, is given by the quantum theory, a branch of physics that underwent great development in the early 20th century. Studying how the atomic scale systems evolve precisely over time by interacting with each other and the environment requires an enormous computational effort. The platforms available today for these types of simulations are predominantly machines that, from a hardware point of view, are largely based on the laws of quantum theory - suffice it to say that semiconductor theory is fundamentally quantum mechanics. However, the type of information that is handled by these computers is purely classical, based on binary systems and classical logic. More generally, all the devices that we find in our daily life are executing algorithms that can be executed on a universal Turing machine, which in turn follows the rules of classical physics (introduction of [1]). Why not try to model these very complex phenomena with the main protagonists of the phenomena themselves, the atoms? In more general terms, is it possible to use quantum mechanical objects to simulate other less-accessible quantum systems? Richard Feynman, in 1982, not only asked himself this very question, but also gave to it a positive answer. He proposed harnessing quantum physics to build a different kind of computer, able to work directly on the wave functions of quantum systems. A historical phrase that is often recalled from one of his speeches [2] is the following:

> Nature isn't classical, dammit, and if you want to make a simulation of nature, you'd better make it quantum mechanical, and by golly it's a wonderful problem, because it doesn't look so easy.
>
> R.P. Feynman, 1982

Certainly, it is not the easiest thing to do. In the years before the 1980s, experiments where it might be possible to precisely control the state of individual atoms with light were considered unfeasible. This scepticism was mainly due to the microscopic size of the objects to be manipulated, and can be summed up by a sentence uttered by Erwin Schrödinger [3]:

> We never experiment with just one electron or atom or (small) molecule. In thought-experiments we sometimes assume that we do; this invariably entails ridiculous consequences... we are not experimenting with single particles, any more than we can raise Ichthyosauria in the zoo.
>
> E. Schrödinger, 1952

However, a few years later in 1989, Wolfgang Paul won the Nobel Prize by suggesting a method for trapping charged particles using variable electric fields [4]. Shortly afterwards, the field of quantum computation began to take hold [5] and one can consider Paul's achievement as one of the milestones on its development. Nowadays, several research fields [1] are active in the realisation of quantum computers, and they are based on a variety of different technologies including superconducting circuits, topological devices, photons, neutral atoms, quantum dots, NV-centers and others [6, 7, 8, 9].

A quantum computer [10] stores the information in a register consisting of quantum objects (qubits). These machines are capable of implementing quantum algorithms with limited errors, corresponding to the quantum mechanical time evolution of the register itself under the action of quantum gates. Problems that are exponentially hard to solve on a classical computer include prime number factorisation and efficient database search, for which possible quantum algorithms exist already [11]. The quantum algorithm to perform prime number factorisation is known as Shor's algorithm [12, 13] (theory and practical implementation) and is almost exponentially faster, in the computation time, than the best known classical factoring algorithm [14]. Richard Feynman also said in a lesson later:

> We are to be even more ridiculous later and consider bits written on one atom instead of the present 10^{11} atoms. Such nonsense is very entertaining to professors like me. I hope you will find it interesting and entertaining also.
>
> R.P. Feynman, 1986

and this is one of the first moments where it is thought that a quantum computer should be used to overcome the paradigms of classical computation in terms of bits. Quantum computers that cannot implement a universal set of quantum gates and have not error-correction capabilities are instead referred to as quantum simulators [15], as they can still solve some specific problems very efficiently. In particular, quantum simulators consist of highly controllable quantum systems used to simulate [16, 17, 18] other, less accessible ones. With quantum simulators, the concept of computation with qubits is relaxed to a more generic encoding of a problem in a quantum register. To conclude this discussion, the box below is intended to give a coarser and more technical understanding of the memory storage required for simulating quantum systems with classical computers.

The qubit (described later in Subsection 1.3.1 more in detail) is the fundamental unit of quantum computation and can be described by a complex wave function of the form $|\psi\rangle = \alpha\,|0\rangle + \beta\,|1\rangle$. In order to study the evolution of a wave function of this kind in a classical computer can be done by firstly storing both complex wave function coefficients α and β and subsequently evolving them according to time-evolution operators. We illustrate this problem in absence of decoherence and with pure states, i.e. in an ideal case. Scaling the problem to a $n \times n$ lattice of qubits, the number of coefficients to be stored amounts to 2^{n^2} for the general case: n^2 entries with a local dimension of $d = 2$ (two states of the qubit) for each. With both 8 bits and 8 qubits, 256 combinations of 1 and 0 can be realised, the difference being that in the second case the 8 qubits can encode them simultaneously, whereas the bits can only represent only one of these combinations [19]. For each coefficient of the overall lattice wave-function to be stored in double precision, one needs 64 bits both for real and imaginary part, so 2^{n^2+4} Bytes. We report some examples for the memory demand in the following table:

lattice dimension	1×1	4×4	8×8
coefficients	2	65.5×10^3	18×10^{18}
state vector	32 B	1 MB	295 EB

In the last case one would require a memory space that is about 850 times larger than the one available at CERN [20]. For a lattice with $n = 17$ the number of bits required to represent all the coefficients of the wave function exceeds the number of atoms in the visible universe by several orders of magnitude, placing an important limit on feasibility. A generic time evolution requires then computationally heavy linear algebra operations.

In 2000, the physicist David DiVincenzo has defined seven criteria that every quantum computer must meet to be defined as such [21, 22]. These principles have always been the beacon for all scientists trying to build a quantum computer, and we illustrate them below while also introducing some insights regarding the platform based on trapped ions:

1. *A scalable physical system with well characterised qubits.*

   Quantum computers based on trapped single ions are among the most promising. In general, the qubits used in such architectures are well characterised via electronic states [23, 24] and in our experiment realised through the $5S_{1/2} \rightarrow 4D_{5/2}$ quadrupole transition of a $^{88}Sr^+$ ion. The biggest challenge facing trapped ions is their scalability, although several proposals have been made in this respect [25, 26]. With trapped ion technology, there have also been recent advances in the area of quantum error correction, by means of ion shuttling techniques [27].

2. *The ability to initialise the state of the qubits to a simple fiducial state, such as $|000\ldots\rangle$.* In the field of quantum information, the fidelity $\mathcal{F}$ is a measure of distance between two quantum states (i.e. the experimentally prepared and ideally prepared state. P. 409 of [1]). $\mathcal{F} > 0.99$ can be achieved preparing the ions in a well-defined electronic state with optical pumping. To be properly initialised, they also need to be cooled to their motional ground state and we will discuss in detail the procedure in Section 2.3.

3. *Long relevant decoherence times, much longer than the gate operation time.*

   A quantum wave-function is said to be in a coherent superposition ($|\psi\rangle = \alpha |\uparrow\rangle + \beta |\downarrow\rangle$) of states if there exist an observable ($\hat{\sigma}_x$) that, if applied to one state, can turn it to another one present in the superposition ($\hat{\sigma}_x |\uparrow\rangle = |\downarrow\rangle$). For a qubit state like $|\psi\rangle$, its decoherence time corresponds to the time at which the off-diagonal terms of its density matrix vanish to zero. The decoherence happens due to interactions of the qubit with the environment, and places an important limit on the capabilities of a quantum computer. In trapped ions, long decoherence times have been reached, even longer than one hour for a particular ion species [28].

4. *A "universal" set of quantum gates.*

   If an arbitrary interaction between any number of qubits can be broken down into a certain set of operations, this set is called universal. In Boolean algebra, the NAND has the property of functional completeness, meaning that any Boolean expression can be recast by an equivalent expression using only NAND operations. In quantum computing, it can be shown that all quantum algorithms can be implemented as a sequence of single qubit and a specific two-qubit operations, thus forming a universal set of quantum gates [29]. Two qubit operations can be for example the controlled-NOT (CNOT) gate [30] or the Mølmer-Sørensen (MS) gate [31, 32]. The MS gate is specific for the case of trapped ions.

5. *A qubit-specific measurement capability.*

   We detect the qubit state through Dehmelt's electron shelving technique, explained in Section 2.2. In a nutshell, one of the two qubit states is excited with laser light to a short-lived auxiliary level from where it decays back to the initial state and emits fluorescence photons. The second qubit state stays untouched and does not emit photons. The fluorescence is then detected via a photo-multiplier tube (PMT) or a camera (Subsection 2.2.1).

And the last two are more related to the branch of quantum communications and networks.

6 *The ability to interconvert stationary and flying qubits.*

   In Quantum Key Distribution (QKD) protocols, photons are used as carriers of the qubit information. The quantum information has to be efficiently transported from the flying photons to the stationary qubit, the ion.

7 *The ability faithfully to transmit flying qubits between specified locations.*

   Photons carrying quantum information can be efficiently transferred between different spatial locations through fibers or in free-space.

Not all the possibilities that quantum computers can offer are explored yet. While still significant improvements have to be made to realise a fault tolerant device, we are within a phase called Noisy Intermediate-Scale Quantum era (NISQ) [33].

The experimental platform at Stockholm University is based on $^{88}\text{Sr}^{+}$ confined in a linear Paul trap. For us, each of the ions belonging to a chain can encode a qubit. The quantum state of each single qubit has to be precisely manipulated. The purpose of this six months thesis project mainly concerns DiVincenzo's fourth criterion and thus a system for the addressing of a chain of ions is described. The task was to use the software Zemax OpticStudio as a reference point to simulate and study different optical setups for addressing qubits with 674 nm laser light, to perform single- and multi-qubit gates. Moreover, it will be shown how the components needed are characterised and then implemented in the actual experiment to achieve the final aim. During the time span of the project, it was possible to test addressed off-resonant single-qubit gates. The thesis is structured as follows:

Chapter 1 The first chapter is related to the theoretical background. Some atomic physics concepts will be briefly introduced and are mainly related to atom-light interaction, along with an explanation of how a Paul trap is able to keep ions stable in a region of space. The last section is devoted to a brief introduction to quantum information concepts.

Chapter 2 In the second chapter, the experimental apparatus is introduced with more technical details on lasers and ion loading. The single-ion addressing apparatus is described and characterised.

Chapter 3 In the last chapter, first results obtained with the new addressing system are presented. It will be described how the addressing quality is optimised and how a single qubit off-resonant gates can be performed on a three ion chain.

Chapter 1

Theoretical background

In this chapter, some important theoretical concepts are illustrated with the aim of allowing the reader to understand the experiments carried out. The physics of Radio Frequency (RF) traps and a summary of the electronic structure of atomic and singly-ionised strontium are given in Section 1.1. Although the description of the trap is more experimental, this topic is included in order to better motivate the emergence of motional degrees of freedom (theory and experiment will be overlaid for a moment). A final discussion is then made on how the light couples to the ion in Section 1.2, and how the different interactions can be exploited to perform quantum computing operations with trapped ions in Section 1.3.

1.1 Trapped ions

In 1953, Wolfgang Paul built the first quadrupolar 3D ion trap [4, 34], with which he later won the Nobel Prize in 1989. This is based on the use of time-varying electric fields to trap charged particles. It should be noted that this is not the only way to trap particles, as different architectures exist (linear, multiple, digital, spherical ion traps), and in others magnetic fields are also used for the confinement (Penning trap [35]).

1.1.1 The ion trap

A macroscopic linear quadrupolar trap (also named as RF trap or Paul trap), confines charged particles in a potential minimum at room temperature using time-varying electric fields. Its physics is well established and there exist several extensive reviews in the literature, such as [36]. The working principle can be initially grasped with the analogy of a ball in a saddle. A ball will start to roll along the negative curvature of the potential landscape if the latter has a saddle shape. This obvious behaviour can be modified by rotating the saddle around the vertical axis that crosses the saddle point. In fact, the inertial mass of the ball introduces a delay in the movement at the right rotation frequency. The curvature changes are so rapid that the ball will be stationary at one point. However, what happens in a real Paul trap is slightly different, since the potential is not rotating, but rather oscillating: slopes become valleys and vice-versa.

Let us now consider an electric potential of approximately quadrupolar shape in the centre

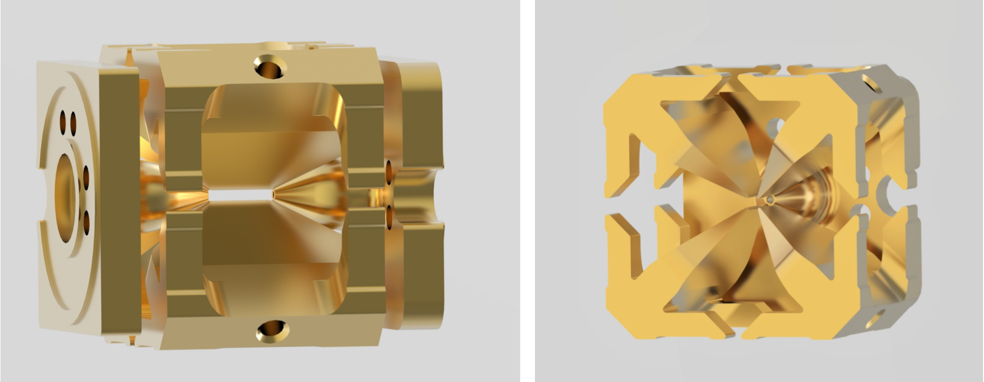

Figure 1.1: A rendering of the Paul trap implemented in our experiment. The electrodes are made of gold-plated titanium [37]. End-cap electrodes are placed at the side of the trap and are easily recognisable by their pointed shape. A hole is drilled in the centre of these to allow laser beams to pass through. The RF signal is instead delivered through the four trapezoid-shaped blades. Pictures are taken from [38].

of the trapping region, such as a generic harmonic potential of the form:

$$\boldsymbol{\Phi} = \Phi(x, y, z) = \Phi_0(\alpha x^2 + \beta y^2 + \gamma z^2), \tag{1.1}$$

where Φ_0 is the field amplitude, and α, β, γ are geometric coefficients related to the trap design. A first major obstacle to the confinement of ions with a similar potential is related to Earnshaw's theorem. The latter states that is not possible to create a potential minimum where the ions can be trapped, by using only static electric fields. To be in equilibrium at a potential minimum, the particle must feel a restoring force that brings it back to its original equilibrium position every time it moves away from it. For a charged particle, this means that the electric field lines have to be directed towards the equilibrium point, and the divergence of the electric field at this point must be negative (the equilibrium point is a sink). The first Maxwell equation forbids it. The last imposes that the field must be divergenceless in the absence of a free charge density $\rho = 0$, and this is the case in an empty trap. The first Maxwell equation has the same structure as the Laplace equation:

$$\nabla \cdot \boldsymbol{E} = \nabla \cdot (-\nabla \boldsymbol{\Phi}) = \nabla^2 \boldsymbol{\Phi} = 0, \tag{1.2}$$

which imposes a condition on the geometric coefficients in Eq. (1.1):

$$\alpha + \beta + \gamma = 0. \tag{1.3}$$

Thus, from the latter one can understand that with only a static field it is not possible to create any confinement: at least in one direction the potential must be anti-trapping, prompting the ion to rapidly escape. If instead this quadrupolar potential is varied it gives rise to a force, which averaged in time is able to push the ion towards the centre of the trap. To realise this dynamical trapping in practice, one can either choose $\alpha = \beta = 1$, $\gamma = -2$ which gives rise to a 3D trap, or $\alpha = -\beta = 1$, $\gamma = 0$ which is instead referred to as the linear Paul trap.

The experiment reported here employs a linear Paul trap (see Figure 1.1) which consists of four gold-plated titanium blades and two end-cap electrodes. The confinement in the plane perpendicular to the trapping axis is generated by a combination of a static and oscillating quadrupole field: $\mathcal{U}(t) = \mathcal{U}_{\mathrm{ST}} + \mathcal{U}_{\mathrm{RF}} \cos(\Omega_{\mathrm{RF}} t)$. The oscillating field is provided by RF voltages applied to a pair of diagonal blades, while the other two are grounded. This potential extends homogeneously along the length of the blades and an additional DC voltage in the axial direction $\mathcal{U}_{\mathrm{DC}}$ is required for three-dimensional trapping. Thus, considering all contributions, the potential takes the following form [39]:

$$\mathbf{\Phi} = \frac{\mathcal{U}(t)}{2r_0^2}(x^2 - y^2) + \frac{\kappa \mathcal{U}_{\mathrm{DC}}}{2z_0^2}(2z^2 - x^2 - y^2), \tag{1.4}$$

where $r_0 = 0.57\,\mathrm{mm}$ [37] is the minimum distance between the trapping axis and the blade electrodes, $z_0 = 2.25\,\mathrm{mm}$ [37] is the minimum distance between the center of the trap and the end-cap electrodes and κ is a geometric factor ($\kappa \approx 0.04$ in our trap [40, 39]).

The behavior of the ion inside the trap can further be investigated by studying the equations of motion along the three axis, given the potential in Eq. (1.4). For a singly charged ion $^{88}\mathrm{Sr}^+$, the equation of motion along the x axis can be written as:

$$\begin{aligned} F = m\ddot{x} = eE &= -e\frac{d\mathbf{\Phi}}{dx} \\ &= -ex\left(\frac{\mathcal{U}_{\mathrm{ST}} + \mathcal{U}_{\mathrm{RF}}\cos(\Omega_{\mathrm{RF}} t)}{r_0^2} - \frac{\kappa \mathcal{U}_{\mathrm{DC}}}{z_0^2}\right), \end{aligned} \tag{1.5}$$

and by performing the substitution $\tau = \Omega_{\mathrm{RF}}/2$, Eq (1.5) can be cast to a generic expression of the Mathieu equations [41]. One then obtains for the three dimensions:

$$\frac{d^2x}{d\tau^2} + (a_x - 2q_x\cos(2\tau))x = 0, \tag{1.6}$$

$$\frac{d^2y}{d\tau^2} - (a_y - 2q_y\cos(2\tau))y = 0, \tag{1.7}$$

$$\frac{d^2z}{d\tau^2} + \frac{2\kappa|e|\mathcal{U}_{\mathrm{DC}}}{mz_0^2}z = 0, \tag{1.8}$$

where the following coefficients have been introduced:

$$a_x = \frac{4|e|}{m\Omega_{\mathrm{RF}}^2}\left(\frac{\mathcal{U}_{\mathrm{ST}}}{r_0^2} - \frac{\kappa\mathcal{U}_{\mathrm{DC}}}{z_0^2}\right), \quad a_x = \frac{4|e|}{m\Omega_{\mathrm{RF}}^2}\left(\frac{\mathcal{U}_{\mathrm{ST}}}{r_0^2} + \frac{\kappa\mathcal{U}_{\mathrm{DC}}}{z_0^2}\right), \quad q_x = -q_y = \frac{2|e|\mathcal{U}_{\mathrm{RF}}}{mz_0^2\Omega_{\mathrm{RF}}^2}. \tag{1.9}$$

The coefficients in Eq. (1.9) are referred to as stability parameters, because a charged particle can experience an average confining force only if these two are inside certain boundaries [42, 43]. In fact, considering that in a linear trap $z_0 \gg r_0$ one approximates $a \approx 0$ and a stable trapping is possible only for $0 < q < 0.9$. The dependence on the ratio $|e|/m$ allows also tuning of the stability parameters (depending respectively on the two voltages) in order to trap only isotopes with a pre-defined charge-to-mass ratio. Solving Eq. (1.6), Eq. (1.7) and Eq. (1.8), one obtains ions oscillating at the following motional frequencies in each of the three axis:

$$\omega_x = \frac{\Omega_{\mathrm{RF}}}{2}\sqrt{\frac{q_x^2}{2} + a_x}, \quad \omega_y = \frac{\Omega_{\mathrm{RF}}}{2}\sqrt{\frac{q_y^2}{2} - a_y}, \quad \omega_z = \sqrt{\frac{2\kappa|e|\mathcal{U}_{\mathrm{DC}}}{m z_0^2}}. \tag{1.10}$$

In the experiment, the trap is typically operated at $a \approx 0$ and $q \approx 0.3$, resulting in trapping frequencies of $\omega_x = \omega_y \sim 2\pi \times 1.7\,\mathrm{MHz}$ and $\omega_z = 2\pi \times 840\,\mathrm{kHz}$ [40]. As a final remark, the trap operates in an ultra-high vacuum regime ($< 1 \times 10^{-10}\,\mathrm{mbar}$) in order to minimize the interaction between the trapped ion qubits and background atoms.

1.1.2 Quantum harmonic oscillator

The Hamiltonian describing the behaviour of a single ion in a one-dimensional (e.g. the x axis) harmonic potential consists of the ion's kinetic energy and its potential energy:

$$\mathcal{H}_m^x = \frac{p_x^2}{2m} + \frac{1}{2}m\omega_x^2 q_x^2 \underset{(a)}{\rightarrow} \hat{\mathcal{H}}_m^x = \frac{\hat{p}_x^2}{2m} + \frac{1}{2}m\omega_x^2 \hat{q}_x^2, \tag{1.11}$$

where in (a) the quantisation technique has been used, introduced by Paul Dirac in 1927 to promote the particle's position and momentum to operators. In the same framework, one can further express the two operators newly introduced in terms of the harmonic oscillator ladder operators of annihilation $\hat{a}$ and creation $\hat{a}^\dagger$. These two, act on the infinite-dimensional Hilbert space $\mathcal{H}^\infty$ of "number representation", called Fock space $\mathcal{F} \subset \mathcal{H}^\infty$. An element of this space has the form $|n\rangle \in \mathcal{F}$, describing the presence of n phonons or quanta of motion. Two elements of this space are orthogonal to each other. The two operators $\hat{a}$ and $\hat{a}^\dagger$ obey the following eigenvalue equations:

$$\hat{a}^\dagger |n\rangle = \sqrt{n+1}\,|n+1\rangle\,, \quad \hat{a}\,|n\rangle = \sqrt{n}\,|n-1\rangle\,. \tag{1.12}$$

The number operator is defined as $\hat{N} = \hat{a}^\dagger \hat{a}$, whose eigenvalues correspond to the number of phonons present in the trap, i.e. $\hat{N}\,|n\rangle = n\,|n\rangle$. As previously described, the newly introduced lowering and raising operators lead to the useful representation of $\hat{p}_x$ and $\hat{q}_x$:

$$\hat{q}_x := \sqrt{\frac{\hbar}{2m\omega_x}}(\hat{a}^\dagger + \hat{a}), \tag{1.13}$$

$$\hat{p}_x := i\sqrt{\frac{\hbar m\omega_x}{2}}(\hat{a}^\dagger - \hat{a}). \tag{1.14}$$

In this way the quantum Hamiltonian in three-dimensions becomes:

$$\hat{\mathcal{H}}_m = \sum_i \hat{\mathcal{H}}_m^i = \sum_i \hbar\omega_i \left(\hat{N}_i + \frac{1}{2}\right) \quad i = \{x, y, z\}. \tag{1.15}$$

The centre of mass of the ion string undergoes a quantized motion in each of the three directions, with the frequencies calculated in Eq. (1.10). More in general, N ions have $3N$ motional degrees of freedom, thus a linear chain has $3N$ eigenmodes of motion with their respective eigenfrequencies. All these modes can be treated as harmonic oscillator modes. The excitation of these motional modes, possible in the Lamb-Dicke regime (described in Subsection 1.2.3), allows the transfer of information, which is shared by all ions in the string, between not nearest neighbour ions. In this way, entanglement gates can be implemented [31, 32]. Motional modes are usually referred as ”quantum buses” to recall their capability to transfer information.

1.1.3 Atomic structure of strontium

Strontium is an alkaline earth metal with 50 neutrons, 38 protons and 38 electrons and an electronic configuration of [Kr]5s^2. In Figure 1.2, the relevant electronic transitions of the atomic strontium are illustrated.

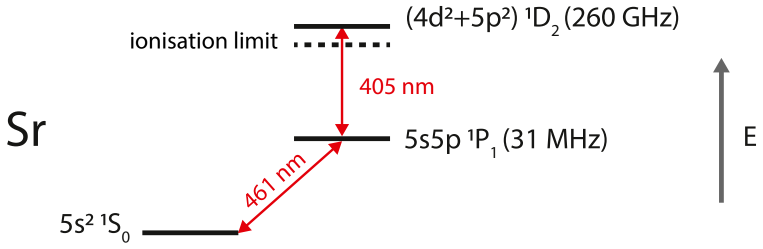

Figure 1.2: Energy levels of ^{88}Sr, relevant for the photoionisation process.

In the experiment, this atomic species is sent through the trap and an electron is removed via a double-step process of photoionisation. The level at the end of this process ($4d^2 + 5p^2$) is doubly excited, meaning that both electrons are still part of the atom (bound), but their combined energy is greater than the first ionisation limit. This state is also called autoionising, and from here one electron falls back to the ground state while the other is ejected into the continuum of unbound states above the first ionisation limit.

At this point, only one electron will be present in the outer shell, and the strontium ion has thus an electronic structure similar to the one of hydrogen. The energy levels can be derived (for a more in depth discussion see section *Single ion theory* from [45]) simplifying the problem from a multi-body one to a nucleus-electron two-body problem. In the latter, the valence electron is confined in a spherically symmetric potential with charge $Z = +2$ (the remaining 36 electrons form closed shells and shield the nuclear charge) and in the external ion-trapping potential. The nuclear spin of this isotope is zero (number of neutrons and protons both even), so it has no hyperfine splitting. The energy levels are further split into $2j+1$ Zeeman sub-levels m_j, ranging from $-$J to J, by means of a permanent magnet generating a magnetic field of $B = 3.6\,\mathrm{G}$ (implemented in [46]).

Starting at the bottom of figure Figure 1.3, the use of all transitions is now described, and details on how they are experimentally driven can be found in Section 2.1. Two Zeeman sub-levels of the metastable state $4D_{5/2}$ and of the ground state $5S_{1/2}$ are identified as the logical qubit states $|0\rangle$ and $|1\rangle$ respectively. These two states are connected through a quadrupole transition (with no P levels in between), which means that the latter has a long lifetime (Table 1.1) and consequently makes this ion a good candidate as an optical qubit. With respect to the bare transition frequency at $B = 0$, the presence of the magnetic field induces shifts in energy levels

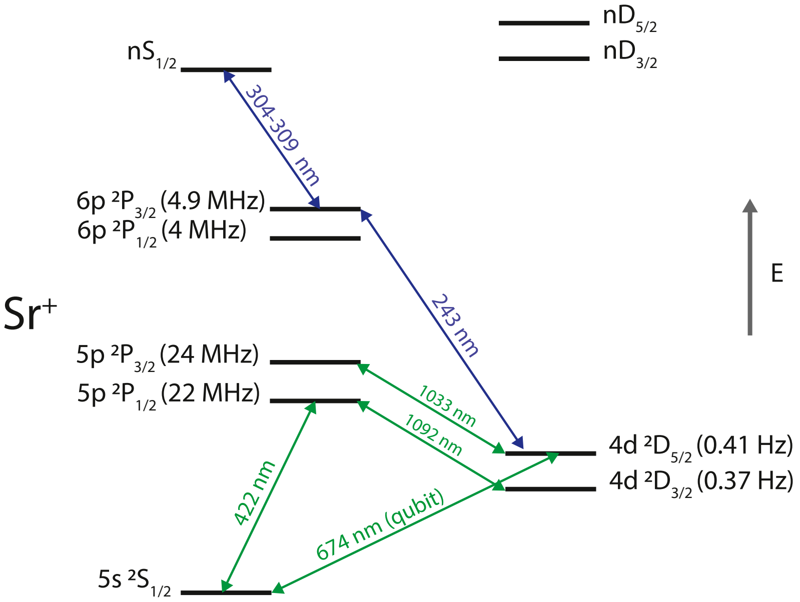

Figure 1.3: Relevant energy levels, including the natural decay rates $\Gamma/2\pi$ [44, 23]. Zeeman sub-levels are not shown for clearer visualisation. The notation used is $\mathrm{nl^{x}\ {}^{2S+1}L_J}$, where $\mathrm{nl^x}$ is the configuration of the outermost orbital (principal quantum number, orbital quantum number and number of electrons in that orbital). Instead, S, L and J are respectively the absolute value of the total electron spin, the total orbital angular momentum and the total angular momentum of the atom (ion). To describe the transitions in the thesis, a more compact notation $\mathrm{nL_J}$ is adopted.

Transition	λ
$5S_0 \leftrightarrow 5P_1$	460.8620 nm
$5P_1 \leftrightarrow 5D_2$	405.2 nm
$5S_{1/2} \leftrightarrow 4D_{5/2}$	674.2064 nm
$5S_{1/2} \leftrightarrow 5P_{1/2}$	421.6711 nm
$5P_{1/2} \leftrightarrow 4D_{3/2}$	1092.7860 nm
$5P_{3/2} \leftrightarrow 4D_{5/2}$	1033.0158 nm

Table 1.1: Wavelengths of atomic and singly-ionised strontium (some low-lying levels) [47, 44, 23].

and consequent shifts in the transition frequencies. Considering, for example, the two sub-levels $m_j(D_{5/2})$ and $m_j(S_{1/2})$, the shift Δ_B can be calculated as:

$$\frac{\Delta_B}{h} = B\mu_B \left[g_J(D_{5/2}) m_j(D_{5/2}) - g_J(S_{1/2}) m_j(S_{1/2}) \right], \tag{1.16}$$

where μ_B is the Bohr magneton, h is the Planck constant and g_J the Landé factor related to a specific energy level:

$$g_J = 1 + \frac{\mathrm{J(J+1) + S(S+1) - L(L+1)}}{\mathrm{2J(J+1)}}. \tag{1.17}$$

Thus, depending on the chosen Zeeman sub-levels, the $5\mathrm{S}_{1/2} \leftrightarrow 4\mathrm{D}_{5/2}$ transition may be more or less sensitive to fluctuations in the external magnetic field. The usual setting is $m_j(S_{1/2}) = -1/2$ and $m_j(D_{5/2}) = -5/2$, but the longest coherence time has been measured with the less sensitive transition between $m_j(S_{1/2}) = -1/2$ and $m_j(D_{5/2}) = -1/2$. From $5\mathrm{S}_{1/2}$, the broad-linewidth transition to $5\mathrm{P}_{1/2}$ (at 422 nm) is also being laser-excited, in order to perform state detection (Section 2.2) and Doppler cooling (Subsection 2.3.1). From $5\mathrm{P}_{1/2}$ the electron does not always return to the ground state $5\mathrm{S}_{1/2}$; rather, there is a 6% [48] probability that it will end up in the metastable state $4\mathrm{D}_{3/2}$ (dark state). To prevent the electron to be trapped in $4\mathrm{D}_{3/2}$ for long, the ”repump” transition (at 1092 nm) from $4\mathrm{D}_{3/2}$ is used, to bring the ion back to the cooling cycle. Lastly, the transition from $4\mathrm{D}_{5/2}$ to $5\mathrm{P}_{3/2}$ (”quench” transition) is used to speed up the resolved Sideband Cooling (SBC), a sub-Doppler cooling technique described in Subsection 2.3.2. This laser is also used to initialize the qubit via optical pumping to the $|1\rangle$ quantum state; in fact, after Doppler cooling the ion ends up in a mixture of the states $m_J = -1/2$ ($|1\rangle$) and $m_J = 1/2$. All the population in $m_J = 1/2$ is then transferred to one of the $4\mathrm{D}_{5/2}$ sub-levels, and with the 1033 nm light subsequently pumped to the ground state. After $\approx 10 - 20$ pump cycles, the ion ends up in $|1\rangle$ with near unit probability.

In addition to low-lying levels, Rydberg energy levels are often used in our laboratory. A two-photon excitation scheme is used to bring the population from either of the metastable 4D states to Rydberg S or D states with $n \approx 46$ [49]. Having discussed how ions can be trapped and what energy levels they consist of, we are now ready to study their interaction with coherent light.

1.2 Interactions

The following paragraphs introduce the Hamiltonian regulating the behavior of an ion trapped in a harmonic potential and coherently manipulated by laser light. First, the manipulation of bare electronic states will be described in Subsection 1.2.1, then motional states will be considered and the coupling to electronic degrees of freedom will be discussed in Subsection 1.2.2. This framework is useful for understanding the quantum operations that are implemented in the rest of the thesis.

1.2.1 Light interacting with a free two-level ion

In the following, a two-level system encoding a qubit is interacting with a laser beam. As a first step in the construction of the overall Hamiltonian, one wants to describe the contribution of the internal electronic structure of the ion. The latter is considered as a two-level system between $|g\rangle$ and $|e\rangle$, separated in energy by $\hbar\omega_0 = \hbar(\omega_e - \omega_g)$ and at a well-defined position in space. This framework is also justified by the fact that in the laboratory light is coupled in resonance only to two internal levels (well enough that couplings to other levels can be neglected, thanks to narrow linewidth lasers). Any operator connected to a two-level system can be mapped onto the spin-1/2 operator basis. In fact, recognizing that:

$$\begin{aligned}
\hat{\mathbb{1}}_2 &= |g\rangle\langle g| + |e\rangle\langle e|, \\
\hat{\sigma}_x &= |e\rangle\langle g| + |g\rangle\langle e|, \\
\hat{\sigma}_y &= i(|e\rangle\langle g| - |g\rangle\langle e|), \\
\hat{\sigma}_z &= |e\rangle\langle e| - |g\rangle\langle g|,
\end{aligned}$$

the two-level quantum Hamiltonian can be written as

$$\begin{aligned}
\hat{\mathcal{H}}_a &= \hbar\omega_g |g\rangle\langle g| + \hbar\omega_e |e\rangle\langle e| \\
&= \hbar\frac{(\omega_e+\omega_g)}{2}(|g\rangle\langle g| + |e\rangle\langle e|) + \hbar\frac{(\omega_e-\omega_g)}{2}(|e\rangle\langle e| - |g\rangle\langle g|) \\
&\overset{(a)}{=} \hbar\frac{\omega_0}{2}\hat{\sigma}_z,
\end{aligned} \tag{1.18}$$

where in (a) the energy has been renormalised to suppress the state-independent contribution.

A monochromatic laser light field, close to the resonance $\omega_\ell \approx \omega_0$ of the $|g\rangle \leftrightarrow |e\rangle$ transition and with a optical phase ϕ_ℓ, can be expressed as $\boldsymbol{E}(t) = \boldsymbol{E}_0 \cos(\omega_\ell t + \phi_\ell)$. Through minimal coupling, both electric dipole, electric quadrupole and even Raman stimulated transitions can be described by the same atom-light Hamiltonian [36]:

$$\hat{\mathcal{H}}_{a\ell}(t) = \hbar\Omega\hat{\sigma}_x \cos(\omega_\ell t + \phi_\ell), \tag{1.19}$$

where the coupling strength Ω is the Rabi frequency. The mechanism of the optical qubit used in our experiment between $5S_{1/2}$ and $4D_{5/2}$ (quadrupole transition) is defined by the interaction of the atomic quadrupole moment with the electric field gradient which is represented in Eq. (1.19). The Rabi frequency is then [50]:

$$\Omega = \frac{e|\boldsymbol{E}_0|}{\hbar}\sqrt{\frac{15\Gamma}{4c\alpha k^3}}\Lambda(m_g, m_e) g_{\Delta_{m_j}}(\phi,\gamma), \tag{1.20}$$

and it is related to the rate at which population is exchanged between $|g\rangle$ and $|e\rangle$ (every $t = \pi/\Omega$ a spin flip happens). In the last equation, $\boldsymbol{E}_0$ is related to the laser intensity $\boldsymbol{E}_0 \propto \sqrt{I}$, $\alpha \approx 1/137$ is the fine-structure constant and Γ is the natural linewidth of the excited state $|e\rangle$. Furthermore, $\Lambda(m_g, m_e)$ is the Clebsch-Gordon coefficient of the transition with Zeeman sublevels m_g (magnetic quantum number) and m_e and the factor $g_{\Delta_{m_j}}(\phi,\gamma)$ contains the geometric dependence of the Rabi frequency, where ϕ denotes the angle between the laser beam and the magnetic field and γ describes the angle between a linear polarisation and the magnetic field vector projected onto the plane of incidence [50]. The complete Hamiltonian is then the following

$$\hat{\mathcal{H}} = \hat{\mathcal{H}}_a + \hat{\mathcal{H}}_{a\ell}(t) = \hbar\frac{\omega_0}{2}\hat{\sigma}_z + \hbar\Omega\hat{\sigma}_x\cos(\omega_\ell t + \phi_\ell). \tag{1.21}$$

At this point, to study the dynamics introduced by the atom-laser Hamiltonian it is convenient to move to the Dirac interaction picture. This hybrid representation is useful to solve problems where the overall Hamiltonian can be rewritten as the sum of a time-independent part and a time-dependent perturbation, as in Eq. (1.21). The dynamics induced by the unperturbed part of the Hamiltonian are detached from those introduced by the time-dependent perturbation, and its solution is generally known. The transformation to the interaction Hamiltonian is performed via

$$\hat{\mathcal{H}}_{int} = \hat{\mathcal{U}}_a^\dagger \hat{\mathcal{H}} \hat{\mathcal{U}}_a,$$

where $\hat{\mathcal{U}}_a = e^{-i\hat{\mathcal{H}}_a t/\hbar}$ is the time evolution operator for the time-independent part. Calling $\Delta = \omega_0 - \omega_\ell$ the detuning between the frequencies of the laser to the atomic transition, the interaction Hamiltonian takes the following form:

$$\begin{aligned} \hat{\mathcal{H}}_{int} &= \hbar\frac{\Omega}{2}\left(\hat{\sigma}_x \cos\left(\Delta t + \phi_\ell\right) + \hat{\sigma}_y \sin\left(\Delta t + \phi_\ell\right)\right) \\ &= \hbar\frac{\Omega}{2}\left(\hat{\sigma}_+ e^{-i(\Delta t + \phi_\ell)} + \hat{\sigma}_- e^{i(\Delta t + \phi_\ell)}\right), \end{aligned} \tag{1.22}$$

where two new operators have been introduced:

$$\begin{aligned} \hat{\sigma}_+ &= \frac{\hat{\sigma}_x + i\hat{\sigma}_y}{2}, \\ \hat{\sigma}_- &= \frac{\hat{\sigma}_x - i\hat{\sigma}_y}{2}. \end{aligned}$$

The former operator pushes the ion's valence electron to the excited level $|e\rangle$, while the latter kicks it down to the ground state $|g\rangle$. In Eq. (1.22) the Rotating Wave Approximation (RWA) has been performed, i.e. the sum of frequency terms $\propto (\omega_\ell + \omega_0)t$ oscillating much faster than the time scale given by the induced dynamics at ω_ℓ is neglected. In the end, the time-evolved quantum state following an interaction $\hat{\mathcal{U}}_1 = e^{-i\hat{\mathcal{H}}_{int}t/\hbar}$ can be written as

$$|\psi(t)\rangle = \hat{\mathcal{U}}_a \hat{\mathcal{U}}_1 \hat{\mathcal{U}}_a^\dagger |\psi(0)\rangle .$$

A distinction must now be made between two cases:

- **On-resonance excitation** ($\Delta = 0$): A laser beam on resonance causes a coherent population exchange between the two energy levels $|g\rangle$ and $|e\rangle$ and can be described by the following unitary operation:

  $$\hat{\mathcal{U}}_1 = e^{-i\hat{\mathcal{H}}_{int}t/\hbar} = \begin{pmatrix} \cos\left(\frac{\theta}{2}\right) & -ie^{-i\phi_\ell}\sin\left(\frac{\theta}{2}\right) \\ -ie^{+i\phi_\ell}\sin\left(\frac{\theta}{2}\right) & \cos\left(\frac{\theta}{2}\right) \end{pmatrix}, \tag{1.23}$$

  where it is convenient to define $\theta = \Omega t$ as the pulse area, quantifying how much the state is being rotated in a time t around a generic axis on the Bloch sphere (see Subsection 1.3.1) $\hat{\sigma} = \hat{\sigma}_x \cos(\phi_\ell) + \hat{\sigma}_y \sin(\phi_\ell)$ defined by the phase of the light ϕ_ℓ. The pulse area also depends on the Rabi frequency, which accounts for the light intensity and coupling efficiency to the corresponding transition. A pulse with duration $t = \pi/\Omega$ is referred to as a $\pi-$pulse. This pulse corresponds in fact to a rotation of 180° on the Bloch sphere: from the south to the north pole of Figure 1.8. One can also notice how in this case the matrix in Eq. (1.23) takes the form of a NOT gate. The continuous application of a laser beam induces a continuous population exchange between the two levels called Rabi oscillations or Rabi flops.

- **Off-resonance excitation** ($\Delta \neq 0$): With laser light detuned from the resonance of the transition there can still be a population exchange between $|g\rangle$ and $|e\rangle$, but suppressed in comparison with the resonant case (see Figure 1.4). By solving the optical Bloch equations (a clear reference with the density matrix formalism can be found at p. 68 of [51]), one finds that the behavior of the probability p_e ($\tilde{\rho}_{22}$ in the reference) of finding the electron in the excited state is governed by the following equation:

$$p_e(t) = \frac{\Omega^2}{\Omega_{\text{eff}}^2} \sin^2\left(\frac{\Omega_{\text{eff}} t}{2}\right). \tag{1.24}$$

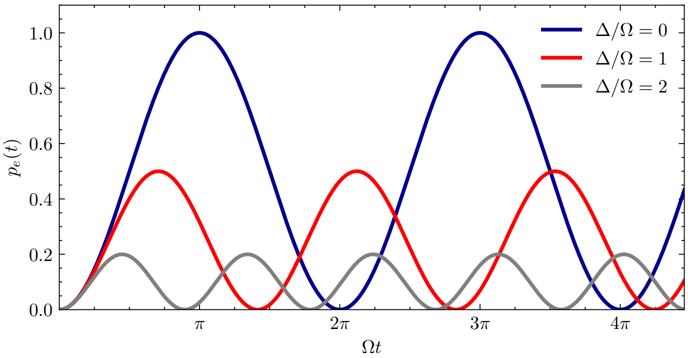

Figure 1.4: Probability of finding the electron in the excited state $p_e(t)$ versus time, at different detuning Δ from the resonance. One may notice how even a non-resonant excitation is capable of generating population transfer between the two energy levels.

Oscillations are performed at the generalised Rabi frequency $\Omega_{\text{eff}} = \sqrt{\Omega^2 + \Delta^2}$ where Ω is the Rabi frequency at resonance. For large detunings $\Delta \gg \Omega$, the oscillations are suppressed (see Figure 1.4) to a reduced amplitude $p_e(t) \propto 1/\Delta^2$.

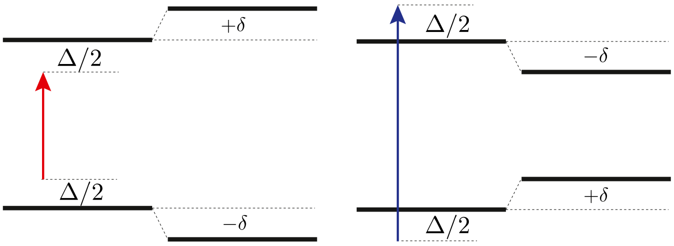

Figure 1.5: Light shift δ of the resonance frequency ω_0 of a transition depending on the detuning $\Delta = \omega_0 - \omega_\ell$. For red-detuned light (frequency of the laser light lower than the one of the transition) the resonance frequency is shifted to a higher frequency, while for blue-detuned light the resonance frequency is shifted to a lower frequency. In case the light is at resonance with the transition ($\Delta = 0$) no light shift occurs.

In addition, a non-resonant light field (detuned by Δ) will shift the atomic energy levels from their original position (AC-Stark shift), as reported in Figure 1.5. To describe this effect, the starting point is again Eq. (1.21). By performing similar steps to those required to obtain Eq. (1.22) considering this time a transformation to a rotating frame with $\hat{\mathcal{U}}_a =$

$e^{-i\omega_\ell \hat{\sigma}_z t/\hbar}$, one can compute the new eigenergies from the following Hamiltonian:

$$\hat{\mathcal{H}}_{\text{int}}^{\text{AC}} = -\hbar\frac{\Delta}{2}\hat{\sigma}_z + \hbar\frac{\Omega}{2}\hat{\sigma}_x. \tag{1.25}$$

By setting $|\hat{\mathcal{H}}_{\text{int}}^{\text{AC}} - \lambda\mathbb{1}| = 0$ one obtains $\lambda_\pm = \pm\frac{\hbar}{2}\sqrt{\Omega^2 + \Delta^2}$. These last two eigenvalues represent the amount of shift that energy levels undergo as a result of the AC-Stark effect:

$$\delta = \lambda_\pm - \lambda_\pm(\Omega = 0) = \pm\frac{\Omega^2}{4\Delta}, \tag{1.26}$$

in the case of large detunings $\Delta^2 \gg \Omega^2$. For this reason, the eigenvalues have been approximated with a first order Taylor expansion of the square root $\lambda_\pm \approx \pm\frac{\Delta}{2}\left(1 + \frac{\Omega^2}{2\Delta^2}\right)$. The sign of the detuning determines the sign of the shift of the levels. As an example, a red-detuned laser $\Delta < 0$ widens the transition, shifting the upper level upwards and the lower level downwards (see Figure 1.5). The overall AC-Stark shift gained in this case amounts to:

$$\delta_{\text{AC}} = \frac{\Omega^2}{2\Delta}. \tag{1.27}$$

So far, the treatment has involved a system with only two levels, but computing the Stark shift in real atoms/ions is more difficult due to off-resonant coupling to all the other energy levels, which for more precise calculation also have to be taken into account. Thanks to the AC-Stark effect, the phase of the qubit will evolve linearly in the pulse duration, allowing us to perform single-qubit manipulations. To see this, from the Hamiltonian in Eq. (1.25) always in the case of large detunings $|\Delta| \gg \Omega$, one can arrive at the following form:

$$\hat{\mathcal{H}}_{\text{eff}}^{\text{AC}} = \hbar\frac{\delta_{\text{AC}}}{2}\hat{\sigma}_z, \tag{1.28}$$

with the related unitary operation

$$\hat{\mathcal{U}}_1 = e^{-i\hat{\mathcal{H}}_{\text{eff}}^{\text{AC}} t/\hbar} = \begin{pmatrix} e^{-i\frac{\delta_{\text{AC}}}{2}t} & 0 \\ 0 & e^{i\frac{\delta_{\text{AC}}}{2}t} \end{pmatrix}. \tag{1.29}$$

Eq. (1.29) is a phase gate (as reported in Eq. (1.46)), in which the qubit phase ϕ rotates linearly in δ_{AC} and in time around the z axis (very similar to the operator that will be presented in Eq. (1.46)). This AC-Stark effect is a key ingredient for single-qubit operations, as will be discussed in Section 3.2.

1.2.2 Light interacting with a harmonically confined ion

The motion of the ion within the trap potential can be described by the quantum harmonic oscillator (see Subsection 1.1.2). This motion affects the interaction between the trapped ion and the laser light, and now the quantum harmonic oscillator and the (free) two-level atom are combined to derive a more thorough description of the system. The latter can be described by

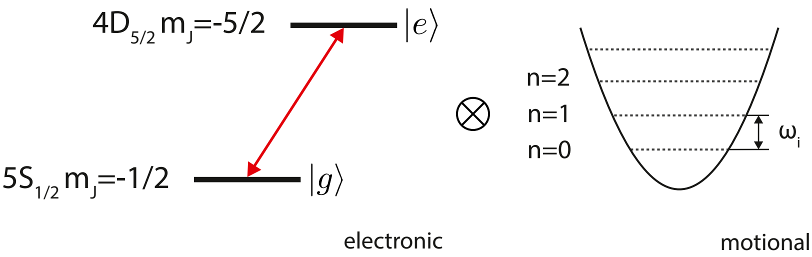

Figure 1.6: The motional and the electronic degrees of freedom are coupled. The axis of quantisation can be identified along $i = x, y, z$.

a Hamiltonian operator that takes into account the following contributions:

$$\hat{\mathcal{H}} = \underbrace{\hat{\mathcal{H}}_m + \hat{\mathcal{H}}_a}_{\hat{\mathcal{H}}_0} + \hat{\mathcal{H}}_{a\ell}(t) = \hat{\mathcal{H}}_0 + \hat{\mathcal{H}}_1, \tag{1.30}$$

where $\hat{\mathcal{H}}_m$ accounts for the motion in the trap (Eq. (1.15)), $\hat{\mathcal{H}}_a$ for the energy stored in the electronic internal levels of the ion (Eq. (1.18)) and $\hat{\mathcal{H}}_{a\ell}$ for the interactions between light and the ion itself. Since the ion is now moving, one must also take into account its spatial position, and for this reason, the Schrödinger position operators $\hat{r}_S = (\hat{x}_S, \hat{y}_S, \hat{z}_S)$ and the wave-vector norm k are inserted in the interaction part (Eq. (1.19)). The calculations can be simplified by considering a monochromatic wave with wave vector lying along the x axis. In this case, the perturbing Hamiltonian is the following:

$$\hat{\mathcal{H}}_{a\ell}(t) = \hbar\Omega\hat{\sigma}_x \cos\left(k\hat{x}_S - \omega_\ell t - \phi_\ell\right). \tag{1.31}$$

The transformed Hamiltonian in the interaction picture $\hat{\mathcal{H}}_{int}(t) = \hat{\mathcal{U}}_0^\dagger \hat{\mathcal{H}}_{a\ell}(t)\hat{\mathcal{U}}_0$, considering $\hat{\mathcal{U}}_0 = e^{-it\hat{\mathcal{H}}_0/\hbar}$ gets the form

$$\hat{\mathcal{H}}_{int}(t) = \hbar\frac{\Omega}{2}(\hat{\sigma}_+ e^{i\omega_0 t} + \hat{\sigma}_- e^{-i\omega_0 t})e^{it\hat{\mathcal{H}}_m/\hbar}\left(e^{i(k\hat{x}_S - \omega_\ell t + \phi_\ell)} + e^{-i(k\hat{x}_S - \omega_\ell t + \phi_\ell)}\right)e^{-it\hat{\mathcal{H}}_m/\hbar}, \tag{1.32}$$

and can be simplified further by neglecting the fast oscillating parts (after expanding the products) and leaving the one which rotates at $\Delta = \omega - \omega_0$ (RWA):

$$\hat{\mathcal{H}}_{int}(t) = \hbar\frac{\Omega}{2}\left(\hat{\sigma}_+ e^{i(k\hat{x}_S - \Delta t + \phi_\ell)} + h.c.\right). \tag{1.33}$$

The position operator $\hat{x}_S$ can be expressed in terms of $\hat{q}_x(t)$, introduced in Eq. (1.13), and so by means of the annihilation and creation operators:

$$k\hat{x}_S = k\hat{q}_x(t) = \eta(\hat{a}(t) + \hat{a}^\dagger(t)), \tag{1.34}$$

where $\eta = |\boldsymbol{k}|\cos(\theta)x_0 = |\boldsymbol{k}|\cos(\theta)\sqrt{\hbar/2m\omega_x}$ is the Lamb-Dicke parameter. The latter includes the angle θ formed between the impinging light and the ion's direction of motion. The final Hamiltonian that regulates the interaction between a trapped ion in motion and laser light is then

$$\hat{\mathcal{H}}_{int}(t) = \hbar\frac{\Omega}{2}\left(\hat{\sigma}_+ e^{i(\eta(\hat{a}(t)+\hat{a}^\dagger(t))-\Delta t+\phi_\ell)} + h.c.\right). \tag{1.35}$$

1.2.3 Lamb-Dicke regime

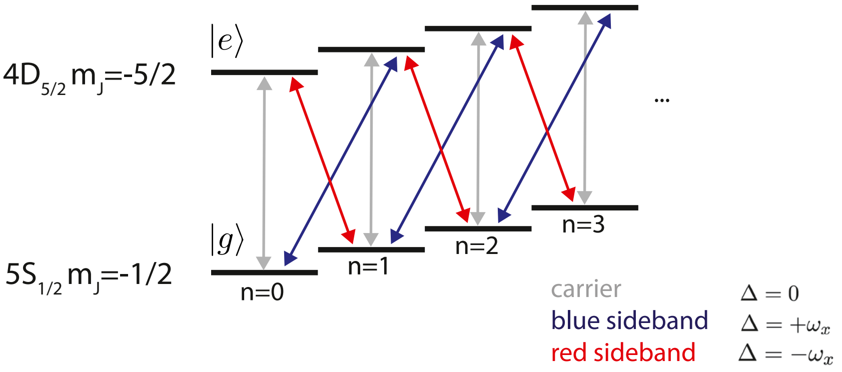

Figure 1.7: Ladder scheme. The carrier transition, driven with a laser not detuned from the atomic resonance, couples the two states $|g\rangle \leftrightarrow |e\rangle$ without affecting the motional state. Starting from state $|g\rangle$, with blue (red) detuned light $\Delta = +\omega_x$ ($\Delta = -\omega_x$) a phonon is added (removed) while the internal electronic state is excited $|g\rangle \leftrightarrow |e\rangle$.

If the extent of the motional wave packet is small compared to the laser wavelength, then an ion is said to be in the Lamb-Dicke regime. Considering $\hat{N}$ to be the number state operator introduced in Subsection 1.1.2, this regime holds as long as $\eta^2(2\langle\hat{N}\rangle + 1) \ll 1$ and is feasible for Doppler-cooled trapped ions whenever the average number of phonons is $\langle\hat{N}\rangle \lesssim 20$. In the Lamb-Dicke regime, the exponent in Eq. (1.35) can be expanded to first order in the Lamb-Dicke parameter:

$$\hat{\mathcal{H}}_{int}(t) = \hbar\frac{\Omega_0}{2}\left(\hat{\sigma}_+ e^{-i(\Delta t+\phi_\ell)}\left[1 + i\eta(\hat{a}e^{-i\omega_x t} + \hat{a}^\dagger e^{i\omega_x t}) + \mathcal{O}(\eta^2)\right] + h.c.\right), \tag{1.36}$$

where the interaction strength is re-scaled by the trap parameter $\Omega_0 = \Omega/(1+q/2)$ (reported in Eq. (1.9)) [52] and where the time dependence of the creation and annihilation operators has been made explicit in terms of the trap frequency. Depending on the detuning Δ from the resonance at ω_0, three different transitions of special interest can be identified in Eq.(1.36) (see also Figure 1.7):

- **Carrier transition** ($\Delta = 0$). This Hamiltonian gives rise to transitions of the type $|g\rangle \otimes |n\rangle \leftrightarrow |e\rangle \otimes |n\rangle$ (resonant light does not cause a change of the number of phonons in the system), with Rabi frequency $\Omega_{n,n} = \Omega_0(1 - \eta^2 n)$:

  $$\hat{\mathcal{H}}_{car} = \hbar\frac{\Omega_{n,n}}{2}(\hat{\sigma}_+ e^{-i\phi_\ell} + \hat{\sigma}_- e^{i\phi_\ell}). \tag{1.37}$$

  One may notice that this Hamiltonian has already been introduced in Eq. (1.22), and that for higher number of phonons $n \gg 1$ the Rabi frequency becomes smaller.

- **Red sideband transition** ($\Delta = -\omega_x$). The result of light with a detuned frequency by a value equal to the trap frequency with respect to the atomic frequency is the excitation of a transition of the type $|g\rangle \otimes |n\rangle \leftrightarrow |e\rangle \otimes |n-1\rangle$. Starting from a state $|g\rangle$, a quantum of motion is removed from the system. The Rabi frequency in this case amounts to $\Omega_{n-1,n} = \Omega_0\sqrt{n}\eta$, and the Hamiltonian takes the following form:

$$\hat{\mathcal{H}}_{rsb} = i\hbar\eta\frac{\Omega_{n-1,n}}{2}(\hat{\sigma}_+\hat{a}e^{-i\phi_\ell} + \hat{\sigma}_-\hat{a}^\dagger e^{i\phi_\ell}). \tag{1.38}$$

This resonance, together with spontaneous decay, is used to perform sideband cooling. This process is described in Subsection 2.3.2 and is useful to cool an ion down to its motional ground state, with $\langle n\rangle \approx 0$.

- **Blue sideband transition** ($\Delta = +\omega_x$). By exciting this transition a quantum of motion is added to the system $|g\rangle\otimes|n\rangle \leftrightarrow |e\rangle\otimes|n+1\rangle$. This excitation is used to prepare arbitrary Fock states of the type $|n\rangle$: after cooling the ion first to its motional ground state $|g\rangle\otimes|0\rangle$, one can apply n times a π pulse on the blue sideband followed by a π pulse on the carrier to return to $|g\rangle$ again with n phonons being added, reaching in the end $|g\rangle\,|n\rangle$. The Rabi frequency is $\Omega_{n+1,n} = \Omega_0\sqrt{n+1}\eta$, and the Hamiltonian for this process reads:

$$\hat{\mathcal{H}}_{bsb} = i\hbar\eta\frac{\Omega_{n+1,n}}{2}(\hat{\sigma}_+\hat{a}^\dagger e^{-i\phi_\ell} + \hat{\sigma}_-\hat{a}e^{i\phi_\ell}). \tag{1.39}$$

In the Lamb-Dicke regime, transitions that change the phonon number by more than one unit are strongly suppressed. In the case of multiple ions confined in the same trapping potential, they influence each other due to their Coulomb interaction. This results in 3N modes, describing the motion of the ion chain in all 3 dimensions. The sideband transitions, as described above, allow one to convert the spin excitation of an ion into a collective motion of the ion chain and to transfer this excitation to any other ion that shares the motional mode. In other words, the motion acts as a bus system, which mediates the interaction between multiple ions in a chain.

1.3 Quantum computation concepts

The purpose of this thesis is to realise a system capable of manipulating individual quantum states of trapped ions. This work opens the door to future quantum information and simulation experiments. The aim of this chapter is thus to introduce the reader to few basic quantum information concepts. There are numerous texts that deal with the subject in greater depth, such as [1].

1.3.1 Pure states

The quantum bit (qubit) is the fundamental and smallest unit of quantum computation. The qubit is defined as a generic two-level (or more, in which case one speaks of quantum dits, or qudits [53]) quantum system, and for this reason it can be encoded in different platforms. For example, the polarisation of a photon or the magnetic flux of a superconducting device can be used to encode qubits. As previously introduced, in our experiment the qubit is encoded

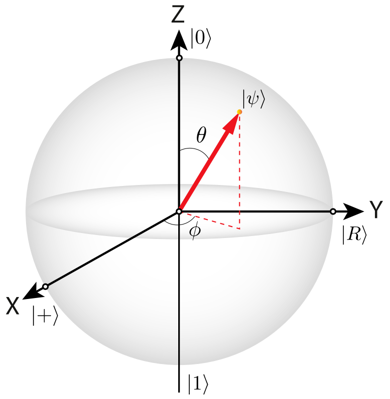

Figure 1.8: Bloch sphere. The vector of a qubit is represented in red, and can reach anywhere on the surface of the sphere. The only information on the Bloch sphere that can be encoded by a bit is the equivalent of $|0\rangle$ or $|1\rangle$. Generally, the Bloch sphere tool is used to visualise single-qubit operations.

between two energy levels of the strontium fine structure. The nature of these objects can solely be explained by the laws of quantum mechanics. The classical counterpart, the bit is also in a sense encodable in any two-level (0 or 1) system (e.g. between two discrete voltage levels of a transistor). The difference between the two, is that in the case of the bit the two levels are two mutually exclusive states, whereas with the qubit these two can both be "occupied at the same time". The two states of the qubit are usually indicated using the Dirac notation as $|0\rangle$ or $|1\rangle$, or equivalently $|\uparrow\rangle$ or $|\downarrow\rangle$. The qubit and its properties are described by its wave-function $|\psi\rangle$. A wave-function representing the pure state of a qubit can be written as:

$$|\psi\rangle = c_{|0\rangle} |0\rangle + c_{|1\rangle} |1\rangle . \tag{1.40}$$

where $c_{|0\rangle}$ and $c_{|1\rangle}$ are two complex coefficients. The complex vector space spanned by $|\psi\rangle$ is generally referred to as Hilbert space $\mathcal{H}$, i.e. $|\psi\rangle \in \mathcal{H}$. The projection postulate from quantum mechanics states that, after the measurement of $|\psi\rangle$ of Eq. (1.40), the system can be either found in $|0\rangle$ with probability $p_{|0\rangle} = |c_{|0\rangle}|^2$ or $|1\rangle$ with probability $p_{|1\rangle} = |c_{|1\rangle}|^2$. Thus, the normalization condition $p_{|0\rangle} + p_{|1\rangle} = 1$ must hold and those probabilities can be only estimated by doing repeated measurements. If N measurements are made, the error that is assigned to the estimate of $p_{|0\rangle}$ and $p_{|1\rangle}$ is the quantum projection noise:

$$\Delta_{p_{|0\rangle}} = \sqrt{\frac{p_{|0\rangle}(1 - p_{|0\rangle})}{N}}, \quad \Delta_{p_{|1\rangle}} = \sqrt{\frac{p_{|1\rangle}(1 - p_{|1\rangle})}{N}}. \tag{1.41}$$

Considering the two states as vectors $|0\rangle = (1,0)^T$ and $|1\rangle = (0,1)^T$, one can rely on a graphic visualisation of the pure state, provided by the Bloch sphere (see Figure 1.8). The qubit state $|\psi\rangle$ can also be defined in terms of the angles ϕ and θ relative to its projection on the x and z axis respectively:

$$|\psi\rangle = e^{i\gamma} \left[\cos\left(\frac{\theta}{2}\right) |0\rangle + e^{i\phi} \sin\left(\frac{\theta}{2}\right) |0\rangle \right] \tag{1.42}$$

where γ is a global phase that can be set to 0 right away as it does not contribute to the probabilities $p_{|0\rangle}$ and $p_{|1\rangle}$. As an example, for $\phi = 0$ and $\theta = \pi/2$ one has the quantum superposition:

$$|\psi\rangle = \frac{|0\rangle + |1\rangle}{\sqrt{2}} = \frac{1}{\sqrt{2}}\begin{pmatrix}1\\1\end{pmatrix} = |+\rangle\,, \tag{1.43}$$

usually referred as $|+\rangle$, a state producing with the same probability $|0\rangle$ or $|1\rangle$ as outcomes of its measurement. Performing gates on a qubit means manipulating its quantum state, by rotating the red arrow in Figure 1.8 on the surface of the Bloch sphere. Considering $\hat{\mathcal{U}}$ to be an operator describing a single-qubit quantum gate, then $\hat{\mathcal{U}}\,|\psi\rangle = |\psi'\rangle$ is nothing but a matrix-vector multiplication, during which $|\psi'\rangle = c'_{|0\rangle}\,|0\rangle + c'_{|1\rangle}\,|1\rangle$ the amplitude coefficients are changed. The only condition on $\hat{\mathcal{U}}$ is that it must be unitary ($\hat{\mathcal{U}}^\dagger\hat{\mathcal{U}} = \mathbb{1}$) to guarantee a reversible computation, i.e. $\hat{\mathcal{U}}^\dagger\,|\psi'\rangle = |\psi\rangle$. The rotations around the three axes x, y, z are described through the three Pauli matrices, forming a basis for the space of 2×2 Hermitian matrices:

$$\hat{\sigma}_x = \begin{pmatrix}0 & 1\\1 & 0\end{pmatrix}, \quad \hat{\sigma}_y = \begin{pmatrix}0 & -i\\i & 0\end{pmatrix}, \quad \hat{\sigma}_z = \begin{pmatrix}1 & 0\\0 & -1\end{pmatrix}, \tag{1.44}$$

whose eigenstates are respectively $|+\rangle$, $|-\rangle$, $|R\rangle$, $|L\rangle$, $|0\rangle$, $|1\rangle$, i.e. the vectors pointing at the intersection of each axes with the Bloch sphere (some are represented in Figure 1.8). The Pauli matrices give rise to three useful classes of unitary matrices when they are exponentiated, as they become rotation operators. In general, a rotation by θ around an arbitrary vector $\vec{n} = (n_x, n_y, n_z)$ can be described by the following operator (p. 174 of [1]):

$$\hat{\mathcal{U}}_{\vec{n}}(\theta) = e^{-i\frac{\theta}{2}\vec{n}\cdot\vec{\sigma}} = \cos\left(\frac{\theta}{2}\right)\mathbb{1} - i\sin\left(\frac{\theta}{2}\right)(n_x\hat{\sigma}_x + n_y\hat{\sigma}_y + n_z\hat{\sigma}_z), \tag{1.45}$$

and, more importantly, an arbitrary single qubit rotation can be decomposed in the following two operators:

$$\hat{\mathcal{U}}_z(\theta) = e^{-i\frac{\theta}{2}\sigma_z} = \begin{pmatrix}e^{-i\frac{\theta}{2}} & 0\\0 & e^{i\frac{\theta}{2}}\end{pmatrix}, \tag{1.46}$$

$$\hat{\mathcal{U}}_\phi(\theta, \phi) = e^{-i\hat{\mathcal{H}}_{int}t/\hbar} = \begin{pmatrix}\cos\left(\frac{\theta}{2}\right) & -ie^{-i\phi}\sin\left(\frac{\theta}{2}\right)\\-ie^{+i\phi}\sin\left(\frac{\theta}{2}\right) & \cos\left(\frac{\theta}{2}\right)\end{pmatrix}, \tag{1.47}$$

where the first operator identifies as a clockwise rotation of an angle θ around the z axis, and the second as a clockwise rotation of an angle θ around an arbitrary axis at an angle ϕ from the $x - y$ plane.

Chapter 2

Experimental setup

In this chapter, the experimental apparatus is introduced. The laser systems are illustrated in Section 2.1 (referring to Figure 1.3. For a more in-depth discussion, especially for the Rydberg part one can read [37]). To slow down the ion in the trap and to initialise it to its motional ground state, Doppler cooling and Resolved Sideband Cooling (SBC) are implemented in the experiment and will be described in Section 2.3. Subsequently, the core of this thesis project is introduced and characterised in its parts, namely the new single-ion addressing system in Section 2.4. The operation of the addressing system is a result of this thesis work. Its description is included in this chapter as it is currently implemented in the experiment.

2.1 Laser system

2.1.1 Optical access

The trap is mounted inside a octagonal chamber, maintained in an ultra-high vacuum regime by an ion pump. The structure has a total of seven viewports and three flanges. The viewports are coated for the different wavelengths used [37]. The way in which the trap is placed inside it, allows access to three different optical axes: one along the axis (axial axis) of the trap through a hole in each of the end-cap electrodes, one perpendicular to the ion chain (radial axis) and a last one at a certain angle in the vertical plane (angled axis), again with respect to the extension axis of the chain. Thus, seven of the ten openings are used to interact with ions, while the remaining for other scopes such as the RF supply or the turbopump. The following descriptions are referring to Figure 2.1.

1. The axial axis, which is perpendicular to the direction of the atomic strontium flow, is primarily used for the photoionisation process. This choice is made because the Doppler effect is small in this direction. The axial beam of ”qubit” laser light at 674 nm also passes through the end-cap electrodes, and interacts with all ions in the chain. This makes it possible to perform global operations on the chain such as on-resonance qubit rotations. Global operations with this laser beam are limited by the fact that there is a maximum momentum transfer with axial movement of the centre of mass of the chain. Since the axial confinement is the weakest among the three axes, the motion along this axis is the one

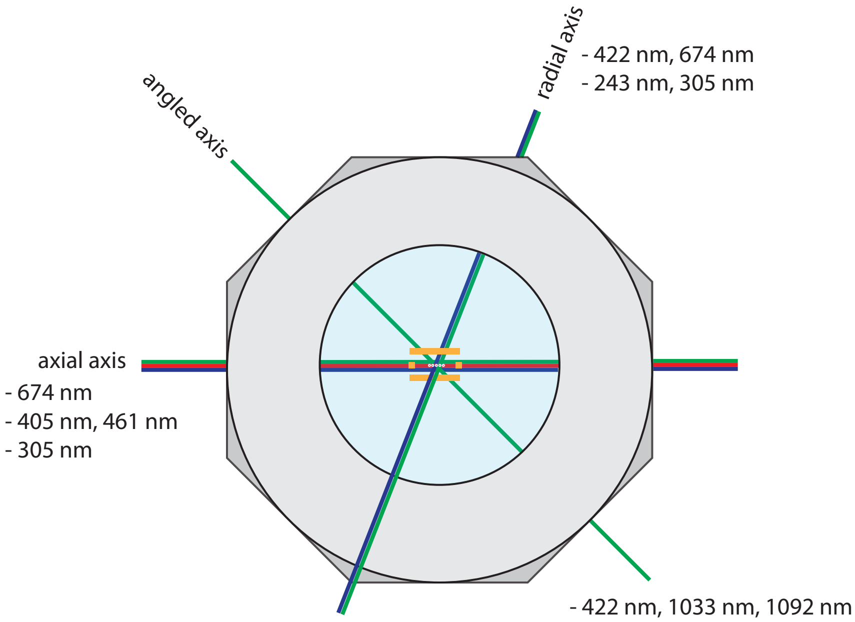

Figure 2.1: Spatial location of laser beams inside the trap. The three main axes, angled axial and radial, are shown. The colours of the beams are chosen to comply with the description of the energy levels in Figure 1.3.

prevailing within the trap. As a consequence, the Lamb-Dicke parameter is large and it therefore becomes complex to drive the sidebands and perform sideband cooling (explained later in Subsection 2.3.2). Moreover, along this axis coherent operations have the shortest coherence time within our setup, and this will be also highlighted in Section 3.2.

2. In the side of the chamber where the ion-addressing system is placed, a high numerical aperture objective lens is mounted. Thus, the radial axis is well suited for single-ion addressing. The objective collects the fluorescence at 422 nm emitted by the ions, directing it towards an Electron Multiplying Charge Coupled Device (EMCCD) camera, and as its focal plane coincides with the ion chain it allows to perform arbitrary operations on single ions, with a radial beam at 674 nm. Since future qubit operations will also be performed on Rydberg states, the objective lens was replaced in this work with one having an additional 305 nm infrared light coating.

3. The angled axis reaches the ions from a viewport located at ≈ 45° on the vertical plane formed with the chain axis. Light passes through this access for laser cooling, at wavelengths of 422 nm 1033 nm and 1092 nm. Thanks to the special angle, the momentum of the photons has a projection along each axis, allowing laser cooling in three directions with a single beam.

2.1.2 Ionisation lasers and ion loading

To obtain and trap strontium ions, a flux of neutral ^{88}Sr atoms can be supplied in two different ways in the center of the trap, and subsequently ionized by photo-ionization. Although it is not the loading process used at present, it is worth mentioning the first method, in which one oven is used to heat up to $T \approx 600\,\mathrm{K}$ the strontium source leaning against it. The heating leads to a cloud of hot atoms, which will diffuse through the chamber to be trapped. To heat up the oven and load an ion takes approximately 15 min. The main drawback of this technique is that it remains warm for several minutes after being switched off, introducing non-negligible black-body radiation. It can be noticed how in this time frame, the frequency of the Rabi oscillations on low-lying levels shifts. Measurements are back to normal only after another 15 min. Pulsed laser ablation loading, implemented by Andreas Pöschl in his master thesis [38] is an alternative to loading from a thermal oven. The atomic flux can be generated almost instantaneously after one strong laser pulse hits the target surface. Moreover, the ablation loading can be activated on-demand and does not heat up the environment around the center of the trap.

The photoionisation process described in Figure 1.2 is also chosen by taking into account the easy commercial availability of lasers at the required wavelengths. The first excitation is given by a laser[1] which provides around 15 mW of light at 461 nm. The second step is driven by a standard laser[2] set at 30 mW of light in output. These lasers hit the ions with a power of $\approx 150\,\mu\mathrm{W}$, that is enough for fast loading (i.e. with < 5 ablation pulses). The two lasers are coupled into the same optical fiber to have them spatially overlapped. Having a narrow linewidth for this two photo-ionisation process is not necessary and so they are not being stabilised to any cavity. It is enough to read the 461 nm light with a wavemeter and change manually the voltage of the piezo of the laser grating, in order to achieve the correct wavelength. A cloud of ions is usually loaded in the trap with less than five ablation pulses. To achieve the desired number of ions, a switch changes the power supply of one of the blades from a 1.5 V battery to a 55 V power supply. In this way, the trap potential is altered and the excess ions are pushed out of the trap along with the hot ions orbiting the centre and not sufficiently cooled.

2.1.3 Manipulation lasers

The light for fluorescence detection and for Doppler cooling is provided by a commercial diode laser[3] at 422 nm. The latter, together with the light at 1092 nm and the one at 1033 nm provided by two commercial lasers[4,5] is stabilized with the Pound-Drever-Hall (PDH) technique to a medium finesse $\mathcal{F} \approx 1000$ cavity. The qubit laser[6] at 674 nm is stabilized with the PDH technique to a high finesse $\mathcal{F} \approx 100000$ cavity, allowing for a linewidth of $2\pi \times 1\,\mathrm{kHz}$. A description is now made of how a single 674 nm beam is split into 3 beams, each reaching the centre of the trap from the 3 different axes. The laser light generated on the laser table is coupled to a fiber to reach the experimental table. Referring to Figure 2.2, a Faraday optical isolator is installed to avoid back-reflections being coupled back into the fiber and interfering with the Fiber Noise Cancellation (FNC) setup placed upstream. By rotating the $\lambda/2$ plates before the PBSs it is possible to decide how much light will be transmitted and reflected, thus changing the powers

---

[1] Toptica DL 100 pro

[2] RGB Lasersystem Lambda beam 405 nm

[3] Toptica DL 100 pro, 50 mW output power

[4] Toptica DL 100 pro, 120 mW output power

[5] Toptica DL 100 pro, 80 mW output power

[6] Toptica DL 100 pro, 500 mW output power

in the three arms. All the 3 AOMs[7] are setup in a double pass configuration and for this reason the frequency shift gained on the 1st diffraction order is double the frequency of the modulator. This arrangement is chosen in order to cancel out the dependence of the deflection angle on the RF frequency applied, and thus avoid alignment issues. In general, the purpose of the 5 lenses present in the setup is to maximize coupling efficiency into the fibers and diffraction efficiencies of the AOMs.

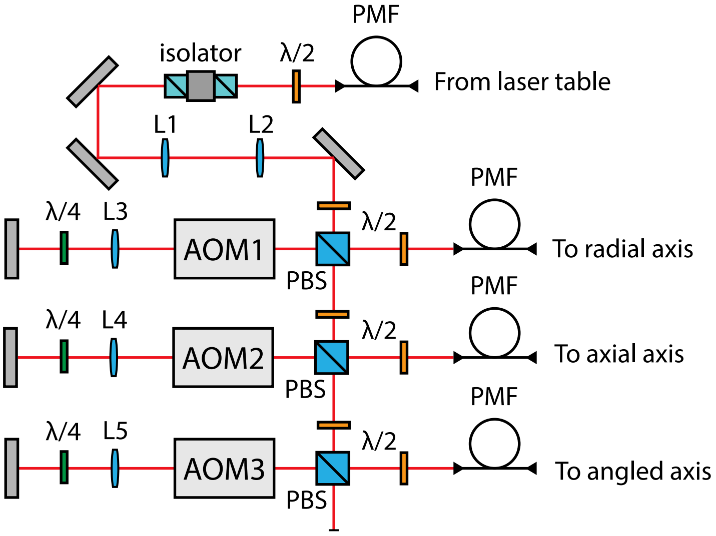

Figure 2.2: A sketch of the splitting optical system. Light on the laser table is coupled to a fiber and reaches the table where the experiment is mounted. With polarisation optics the light intensity is deliberately divided on the three axes. The setup is flexible and allows for different powers according to need.

2.2 Quantum state detection

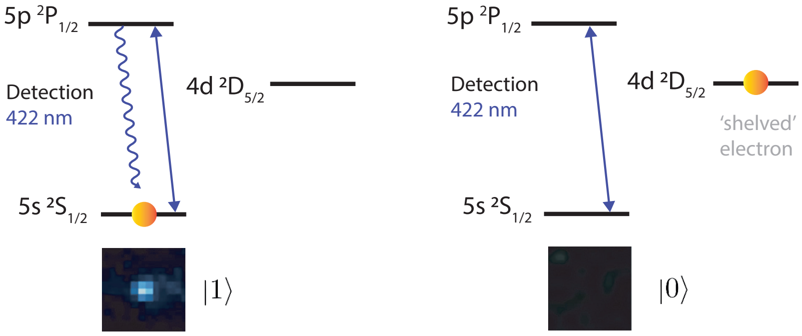

Figure 2.3: Quantum state detection through the electron shelving technique. When the electron is in the ground state, fluorescence light at 422 nm will excite the transition to the short-lived P state. Photons are scattered due to spontaneous emission and the ion is visible (the quantum state associated is thus $|1\rangle$). If instead the electron is in the D state, the detection transition does not scatter any photon and the corresponding quantum state is $|0\rangle$.

The quantum state of the ions must be reliably determined during each instant of the ex-

---

[7] Gooch & Housego 3200-125, $\lambda = 470\,\text{nm} - 690\,\text{nm}$, $f_{\text{RF},c} = 200\,\text{MHz}$, $\Delta f_{\text{RF}} = 50\,\text{MHz}$

perimental sequences. Via the $5S_{1/2} \leftrightarrow 5P_{1/2}$ transition, a single ion can scatter several millions of photons per second (p. 13 of [38]) and a sufficient fraction of them should be enough to be detected even by a detector with a low quantum efficiency. The technique involved in the quantum state detection is called electron shelving [36] and is implemented to distinguish an ion in state $4D_{5/2}$ from an ion in states $5S_{1/2}$ or $4D_{3/2}$ (see Figure 2.3). It works as follows: if the electron is in the $5S_{1/2}$ state, it will be excited to $5P_{1/2}$ and the ion will spontaneously emit photons in all directions. The ion in this state is visible, and for this reason is usually referred to as being in the optical qubit state $|1\rangle$. If instead the electron is in the $4D_{5/2}$ state then it will not scatter photons and the ion will appear 'dark'. For this reason, this state will be assigned to $|0\rangle$. Two different detection techniques are used in our experiment and rely on the electron shelving method just described. The commonly used one is based on a photo-multiplier tube[8] (PMT), which collects the fluorescence light emitted by one or more ions present in the trap. The photons scattered during the electron shelving measurements by the ion, are focussed through an aspherical lens (covering $\approx 2.1\,\%$ of the solid angle) onto a photo-multiplier tube (PMT). In principle, measuring for a time of 500 µs (a time exceeding the lifetimes of all the electronics states except the 4D metastable states and the ground state) allows to distinguish between $|0\rangle$ and $|1\rangle$ with $\approx 99.9\,\%$ of efficiency [49]. As an example, in Figure 2.6 a detection time of 800 µs is used. The second detection method is instead based on an Electron Multiplying Charge Coupled Device (EMCCD) camera[9] and some time was spent on writing functional software to acquire signals from individual ions in the chain. Since measurements in quantum mechanics are inherently probabilistic, each measurement that is made is the result of an N number of measurements. In experimental jargon, N is also referred to as the number of cycles. The averaged result of the measurements is associated with the error introduced in Eq. (1.41). Pulsed-type laser light is used for rapid measurements.

2.2.1 EMCCD camera detection

A threshold based detection with the PMT works well for one or two ions, but cannot determine the quantum state of an ion string. In general, this method cannot give spatial information of individual ions. For this purpose, a back-lit EMCCD camera is used to spatially resolve the ions and study their individual excitations. The same technique, i.e. electron shelving, is used in this context for each ion individually. Since the spatial extension of a cold ions' wave function (< 30 nm for an ion in motion) is typically smaller than the wavelength of the fluorescence light (≈ 422 nm for our ion species), single ions show up as bright dots with a size determined by the resolution limit of the imaging optics. Once the new apparatus was mounted, the pixel-distance conversion between the ions had to be recalibrated. This is because, although very similar to the one previously installed, the magnification of the new objective lens is different after replacement. In addition, in this thesis work, it was also necessary to replace two lenses in the imaging apparatus. With this change, the simulated distances are better respected and thus aberrations have consequently been reduced and the spacing between ions improved (it

---

[8] Hamamatsu Photonics H10682-210

[9] Andor iXon3 897: 512×512 active pixels, $16\,\mu\text{m} \times 16\,\mu\text{m}$ pixel size, $90\,\%$ QE at 674 nm.

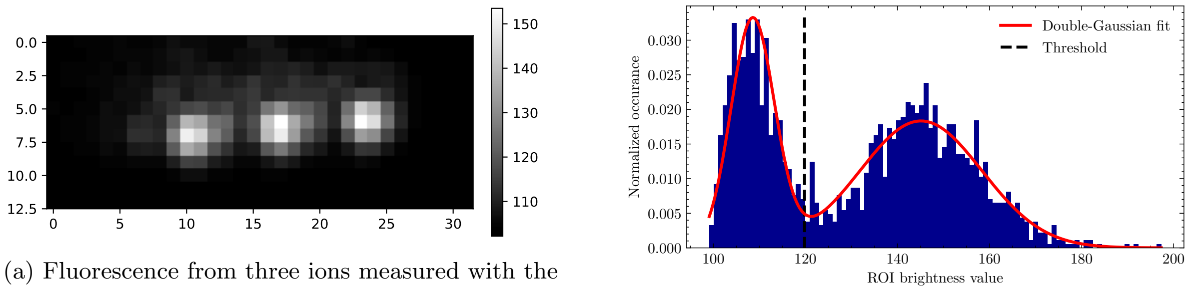

(a) Fluorescence from three ions measured with the EMCCD camera and averaged over an experimental sequence.

(b) Background and signal histogram with crossing point.

Figure 2.4: (a) A picture of three ions, obtained averaging 5100 images taken in an experimental sequence. As explained in Subsection 2.2.1, this imaged is used to locate the position of ions in the sensor. (b) The histogram with the averaged brightness of the ROIs around one of the three ions for each collected image. The data is taken from the central ions of (a), which underwent Rabi oscillations.

is important to note that this is decisive for the analysis of the quantum state of individual ions). No further details on the imaging system optics will be given. To estimate the distance between two ions on the EMCCD camera, the actual distance between them in the trap and the magnification of the imaging system should be known. Numerical calculations of the distance of two (or more) trapped ions for a given axial confinement is calculated following [50, 54]. As explained in Subsection 1.2.2, in the Lamb-Dicke regime the separation between the resonance frequency and the motional sideband is exactly equal to the trap frequency. Therefore, by measuring the gap between the carrier frequency and the one of the axial motional sideband is possible to estimate ω_z. After loading two ions we measure an axial trapping frequency of $\omega_z = 2\pi \times 1.0254\,\mathrm{MHz}$. A theoretical spacing of $d_{\mathrm{real}} = 4.24\,\mu\mathrm{m}$ is computed between the two ions. Subsequently, 200 images of the two stationary ions are collected with the camera and the pixels of all of them are averaged in time. From the resulting image, the distance in pixels is found to be $d_{\mathrm{pixels}} = 96\,\mu\mathrm{m}$. The magnification M is then given by

$$M = \frac{d_{\mathrm{pixels}}}{d_{\mathrm{real}}} \approx 22.6. \tag{2.1}$$

The ion chain can be moved along the longitudinal axis by varying the voltage of the end-cap electrodes along the trap axis $\mathcal{U}_{DC}$. Therefore, it is interesting to know the distance by which they are shuttled, following a 1 V change of either of the voltage. Adopting a method similar to that used to compute the magnification, it can be estimated that a 1 V change of one of the two end-cap electrodes corresponds to $\approx 0.13\,\mu\mathrm{m}$ of ion displacement in the trap. In the future, it can be measured more accurately by means of a linear regression. This will be useful in Section 2.4.2 to determine the laser beam spot-size using just a single ion.

The procedure used to measure the quantum state of each ion is now described. A Python code post-processes the images taken during an experimental acquisition. As a first step, the position of the ions is found. For this, all the images acquired are averaged in time and the x-y location of the N (in the case of N ions) brightest pixels is saved. Then, for each image saved during the acquisition, a region of interest (ROI) of 3×3 pixels is averaged around for each of the N positions found previously. The ROI dimension can be changed and is set to 3×3, as this roughly correspond to the spatial extension in pixels of the ion, and is not including light collected from neighboring ions. If the value of this average is above a certain threshold then the ion is in the quantum state $|1\rangle$, otherwise it is in $|0\rangle$. After saving all the average brightnesses of each ROI, a histogram is fitted Figure 2.4 (b) with a double-Gaussian profile. The point where the two distributions cross will be taken as the threshold for the quantum state detection in order to minimise the labeling error of each data point. A higher single-shot readout fidelity can be reached with a further optimisation of the imaging optics and with the implementation of more complex algorithm [55].

2.3 Laser cooling

It is not possible to trap an ion in the minimum of a potential without first reducing its kinetic energy. Moreover, in order to reliably perform reproducible qubit manipulations the ion needs to be close to its motional ground state. A direct consequence of the confinement, together with the momentum-position uncertainty principle, is that ions cannot be completely at rest. There exist a number of different techniques to reduce their kinetic energy, but only inelastic scattering of laser light makes it possible to cool ions to their motional ground-state. Two techniques under the umbrella of laser cooling [56] are implemented in our experiment: Doppler and resolved sideband cooling (SBC). The two processes just introduced are crucial at the beginning of each experiment run.

2.3.1 Doppler cooling

Doppler cooling is the most commonly used method in laser cooling [57] and also the first step of the cooling process in our experiment. Unless other techniques are implemented, without Doppler cooling it would not be feasible to slow down the motion of the ions during loading. The Doppler effect is the change in frequency of a wave in relation to an objective who is moving relative to the wave source at a velocity v. To carry out this type of laser cooling, the $5S_{1/2} \leftrightarrow 5P_{1/2}$ transition is driven in our experiment. If laser light is shone with a frequency tuned slightly below (red detuned) the one of this electronic transition and the ion is at rest, nothing will happen. On the other hand, especially due to the ionization process, the ion is very energetic and moves very fast in the trap. In this case, when the ion is directed towards the laser beam, the Doppler effect will compensate for the missing frequency gap to drive the transition: an absorption event happens and the atom loses a momentum equal to the one of the photon. An ion moving with a velocity v with respect to the source will experience a frequency shift on the incoming light due to the Doppler effect and will absorb a photon only if

$$\omega_0 = \omega_\ell \left(1 \pm \frac{v}{c}\right) \tag{2.2}$$

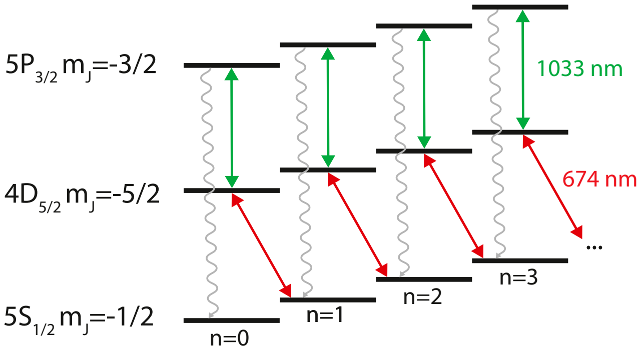

Figure 2.5: Scheme for SBC. A closed cooling cycle can be achieved with light at 674 nm and 1033 nm. Starting from a generic $|g\rangle \otimes |n\rangle$, red detuned light at 674 nm couples the transition to $|e\rangle \otimes |n-1\rangle$. Subsequently, a laser beam 1033 nm is used to drive the level $4D_{5/2} \leftrightarrow 5P_{3/2}$. Thanks to the shorter lifetime of $5P_{3/2}$ the population decays quickly into $|g\rangle \otimes |n-1\rangle$. The procedure is repeated until $|g\rangle \otimes |0\rangle$ is reached.

is satisfied. The atom, being now in the excited state, will emit a photon in a arbitrary direction (spontaneous emission) to return to its energy-efficient configuration. The net effect after many of these events, due to the fact that the momentum of the absorbed photon is given up again along a random direction, is that the kinetic energy of the ion is reduced to the Doppler limit, or that there is no average momentum gain. The minimum temperature that can be reached (in the case where $\omega_z \ll \Gamma_D$) is also defined as the Doppler limit:

$$T_D = \frac{\hbar \Gamma_D}{2k_B} = 0.48\,\text{mK}, \tag{2.3}$$

where it has been considered that the cooling transition, red-detuned from $5S_{1/2} \leftrightarrow 5P_{1/2}$ has a broad linewidth, as reported in Table 1.1. Knowing that laser cooling gives in general a thermal distribution of phonon states [58], one can also compute the mean oscillation quantum number along the three quantisation axis from the following equation:

$$\langle E_i \rangle = \left(\langle n_i \rangle + \frac{1}{2} \right) \hbar\omega_i = \frac{\hbar \Gamma_D}{2} \Rightarrow \langle n_i \rangle = \frac{1}{2} \left(\frac{\Gamma_D}{\omega_i} - 1 \right). \tag{2.4}$$

Considering the trapping frequencies listed at the end of Subsection 1.1.1, easily reachable number of phonons are $\langle n_x \rangle = \langle n_y \rangle \approx 5$, and $\langle n_z \rangle \approx 11$. Usually, Doppler cooling is carried out for 1 ms. At the end of this process $\langle n_z \rangle \approx 16$ and $\langle n_x \rangle = \langle n_y \rangle \approx 12$ have been measured [49].

2.3.2 Resolved sideband cooling

By means of Doppler cooling alone is not possible to reach the ion's motional ground state, since the Doppler limit (Eq. (2.4)) sets a fundamental boundary on the minimum temperature achievable. However, with Doppler cooling is possible to cool the ion down to the Lamb-Dicke regime, where the motional sidebands are resolved from the carrier (Subsection 1.2.3). The assumption made here is that the ion is in a state like $|g\rangle \otimes |n\rangle$, i.e. in the electronic level at lower energy $|g\rangle$ and with n motional phonons. With slightly red-detuned 674 nm light, the ion is brought into $|e\rangle \otimes |n-1\rangle$, which subsequently decays into $|g\rangle \otimes |n-1\rangle$. The last decay is sped up by coupling the $5S_{1/2} \leftrightarrow 4D_{5/2}$ transition with the "quench" laser at 1033 nm (see Figure 2.6). In fact, an electron in $5P_{3/2}$ has a radiative lifetime of 6.653(71) ns compared to the one of the $4D_{5/2}$ state which amounts to 0.3945(23) s [47]. A phonon is lost at each iteration of this process, and by repeating it several times the motional ground state can be reached. On the left-hand side of Figure 2.6, one can see how at the end of the SBC cycle (blue curve), it is no longer possible to drive the red sidebands. Note how the coupling to the red sideband, $\Omega_{n,n-1} = \Omega_0 \eta \sqrt{n}$, tends to 0 with when $n \to 0$. After this procedure, the measured mean phonon numbers are $\langle n_x \rangle = \langle n_y \rangle \approx 0.2$ and $\langle n_z \rangle \approx 0.05$. In part (b) of Figure 2.6 it is shown how longer coherence times in the Rabi oscillations of an ion with fewer phonons can be reached. The information exchanged with the environment can be quantified in terms of energy. A less energetic ion is then exchanging less information and thus the coherence time is extended as a consequence of this. As a final remark, the measurement shown in Figure 2.6 are made with the angled beam.

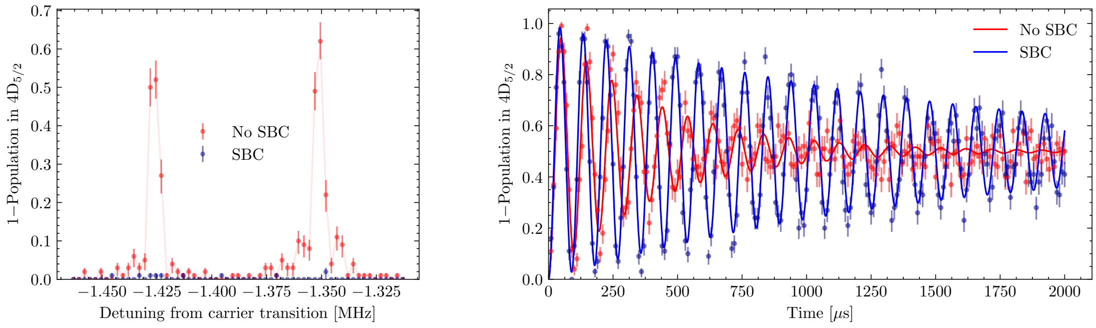

(a) Red sidebands, with and without sideband cooling.

(b) Rabi flops, with and without sideband cooling.

Figure 2.6: (a) A graph showing the red sidebands. They can be driven (red curve) only if the ion is not in the motional ground-state. The blue dots correspond to the motional sidebands when the ion is at $n = 0$. Since the frequency scan (AOM3 in Figure 2.2) is done with the angled beam, the two sidebands correspond to the two oscillation modes along x and y. (b) Rabi oscillation with SBC and without. The coherence times, considered as the point when the population reaches $1/e$ are $\tau_1 = 417(23)$ µs and $\tau_2 = 1578(69)$ µs in the two cases.

2.4 Single-ion addressing system

The quantum state of each individual ion has to be manipulated very precisely in order to perform high-fidelity single qubit operations. To do so, two solutions exist. In one approach, the ions are shuttled in the trap by changing the voltage on the end-cap electrodes $\mathcal{U}_{DC}$. In this way, the ions are moved into the tight focus of a fixed laser beam. However this method has some drawbacks and limitations. For example, shuttling the ion in the trap adds phonons to the system and with such system only one ion can be addressed at a time. In a second approach instead, the laser beam is deflected such that it is focussed on the selected ion. The way the addressing was done prior to this thesis project involved the use of two different parallel laser beams directed towards the centre of the trap, and the ions are moved around in it, following

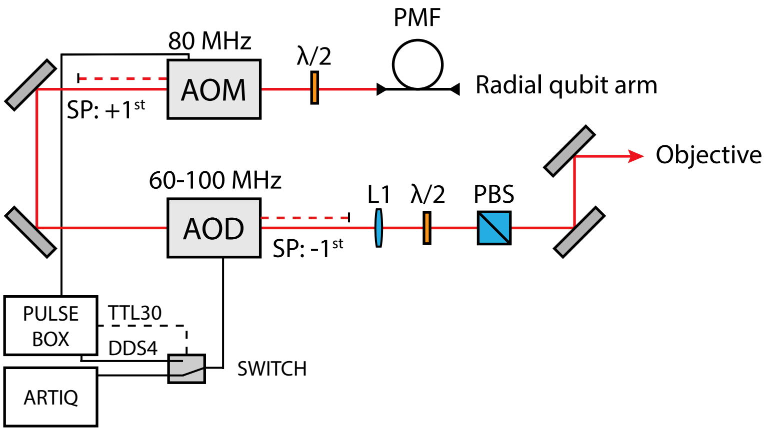

Figure 2.7: A sketch of the addressing setup that will be describe in the next paragraphs. The most important component is the AOD itself, which is powered by two different sources for the reason explained in Section 2.4.3

the first method. In this thesis project, the second approach is adopted, and the laser beam is deflected thanks to an acousto-optic deflector (AOD). Referring to Figure 2.7, the collimated light coming out from the fiber coupler has a diameter of 820 µm and is directed towards the first AOM[10] by means of two mirrors. The reason why this component is included in the system is to compensate for the 80 MHz shift introduced downstream by the AOD. It is in fact not possible to carry out this compensation with the double pass setup for the radial beam in Figure 2.2 as AOM1 would have to operate outside its bandwidth. The polarisation selected by means of the $\lambda/2$ plate is vertical, as specified in the modulator datasheet to maximise the diffraction efficiency.

In the following sections, the requirements that the single-ion addressing setup must meet are illustrated. A simulation with Zemax OpticStudio is presented in the first section. Considering the setup mounted in a different optical table rather than on the experiment, the characterisations of the objective lens and the AOD are reported in Subsection 2.4.2 and in Subsection 2.4.3. The performance of the system in carrying out off-resonant qubit gates will be examined in Chapter 3. A picture of the final setup mounted on the experiment can be found in Figure 3.1.

2.4.1 Zemax simulation

Constraints on the single-ion addressing are mainly dictated by the type of research to be done by the group in the future. It must also be taken into account that another apparatus for single-Rydberg-ion addressing will be mounted in the same area of the experiment, so spacing issues are an important concern. Since the objective has also an imaging purpose, the optical path for collecting the light fluorescence is partially overlapping with the one of the addressing and this limits the available space even more. Moreover, the addressing setup must be able to precisely manipulate the individual qubits in a chain of at least 10 ions. To avoid cross-talking between nearest neighboring ions the spot size must be below 3 µm (considering a trap operated

---

[10] Gooch & Housego 3080-125, $\lambda = 515\,\mathrm{nm} - 633\,\mathrm{nm}$, $f_{\mathrm{RF},c} = 80\,\mathrm{MHz}$, $\Delta f_{\mathrm{RF}} = 25\,\mathrm{MHz}$

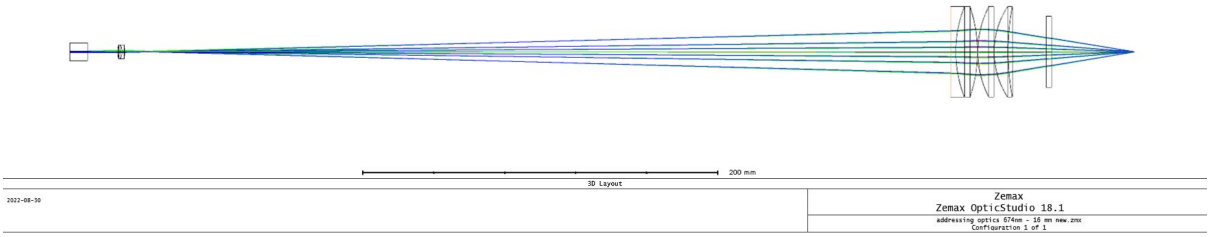

Figure 2.8: The 3D layout of the final addressing setup simulated with Zemax OpticStudio and described in Subsection 2.4.1.

under normal conditions). At the same time, the objective's aperture should be illuminated as much as possible in order to reduce the dimension of the Airy disk, with the restriction that the beam does not get clipped at the maximal and minimal deflection angle. The idea is therefore to simulate with Zemax OpticStudio a setup that is able to meet all these requirements.

Referring to Figure 2.8, the first component is a 1 cm thick piece of TeO_2 crystal and represents the AOD birefringent crystal. From here, three light fields depart at three deflection angles that can be provided by the AOD (0°, 0.7° and 1.4°) when driven by three different RF frequencies. The beams are defined by their entrance pupil diameter with an aperture of 840 µm, that corresponds roughly to the measured spot size of the Gaussian beam before the AOD in the real setup. The maximal deflection angle is 1.4°, which corresponds to a 2.8° scan angle that is close to the one specified on the AOD's datasheet of 3.08°. At $d_1 = 16.9\,\mathrm{mm}$ an aspherical lens[11] is placed in order to expand the beam and match the aperture of the objective lens as much as possible. The objective itself is placed at $d_2 = 465.7\,\mathrm{mm}$ from the lens. One may notice how $d_1 \approx f$ so that the AOD aperture can be imaged on the objective lens, and thus prevent the laser beam from clipping on the optics at large deflection angles. The optimisation of the distances in the simulation is made by fixing the distance between the fused silica viewport and the ion position to $d_4 = 47\,\mathrm{mm}$ ([37, 38] and old lab-books). For completeness, the optimised distance between the last surface of the objective lens and the viewport is $d_3 = 21.5\,\mathrm{mm}$. This simulation returns a similar spot-size for the three beams of 2.6 µm and an addressing range of 128 µm. We expect that with this design all the requirements will be met.

2.4.2 Objective lens characterisation

One single objective lens is used both for imaging and addressing the ions with the light for qubit manipulation (red light at 674 nm) and for Rydberg excitations (ultraviolet). In Figure 2.8 the objective is the ensemble of lenses on the right, and it can also be seen in the long exposure (Figure 6) when is invested by red light. The objective lens was designed by Markus Hennrich and it consists of four 2-inches lenses. It can collect light with a numerical aperture of NA = 0.24 and is placed outside the vacuum chamber, focusing light on the ions through a fused silica viewport. Thanks to its special design, the spherical aberrations introduced by the viewport are compensating for the one introduced by the objective. During the characterisation of the objective lens, it has been noticed how the silicon viewport introduces also a focusing effect.

---

[11] Thorlabs AC080-016-A, $f = 16\,\mathrm{mm}$

For imaging, it is very important that the lenses perform close to the limit imposed by the diffraction (Section 2.4.2). This is the only way to ensure that the optical instrument is able to produce images with a resolution close to the theoretical limit of the instrument, which in turn is designed to clearly resolve individual ions.

The transmission efficiency of the lenses ensemble is also measured. Lenses have a refractive index not perfectly equal to one and this results in a first contribution to the incomplete transmission of the beam. The transmission coefficient is made smaller due to effects like Fresnel reflections and absorption of not perfectly transparent materials. Thus, measuring the efficiency consists in computing the ratio between the input power and the output power of laser beams passing through the objective. The estimates are for beams hitting the centre, the left and the right side of it. They amount to respectively 92 %, 95 %, 96 %. The efficiency on the border is higher due to the fact that there is less glass in the path of the light, and thus less absorption. This lens will also be used to address the ions with UV light at 305 nm, and the measured efficiency at this wavelength amounts to 88 % in the centre.

Diffraction limit

We now characterise the imaging capabilities of the objective. This is done by measuring how well it can resolve two close-lying objects placed in the object plane. The German physicist Ernst Abbe realized that the resolution of an imaging instrument is not constrained by the quality of the instrument, but by the wavelength of light used and the aperture of its optics [59]. Diffraction effects come into play each time an obstacle is placed in the path of the light, selecting only a portion of the wavefront. The nature of diffraction patterns depends on the properties of the gap, and as this approaches the wavelength of the wave, the distortion becomes even more obvious. Because the high frequency components that give an image its sharpness are lost due to this phenomenon, this leads to a fundamental limitation in instrument resolution: the diffraction limit.

The Modulation Transfer Function (MTF) is used to describe the contrast, or modulation of an image, meaning how well patterns of different periodicities (e.g. a series of alternating light and dark bars of equal width) can be resolved by an imaging system [60]. For each of them the modulation M (or visibility), is given by

$$M = \frac{I_{\text{max}} - I_{\text{min}}}{I_{\text{max}} + I_{\text{min}}}, \tag{2.5}$$

where I_{max} is the maximal brightness of a line and I_{min} is the one of the space in between (see Figure 2.9). Since the modulation is dependent on the resolution of the optical system $M = M(v)$, this is linked to the distance between the lines being imaged v. Thus, the MTF is a function of the spatial frequency, where the spatial frequency v is given by the line pairs per millimeters in the object. The MTF then takes the form:

$$\text{MTF}\,[\%] = \frac{M(v)}{M(0)} \cdot 100, \tag{2.6}$$

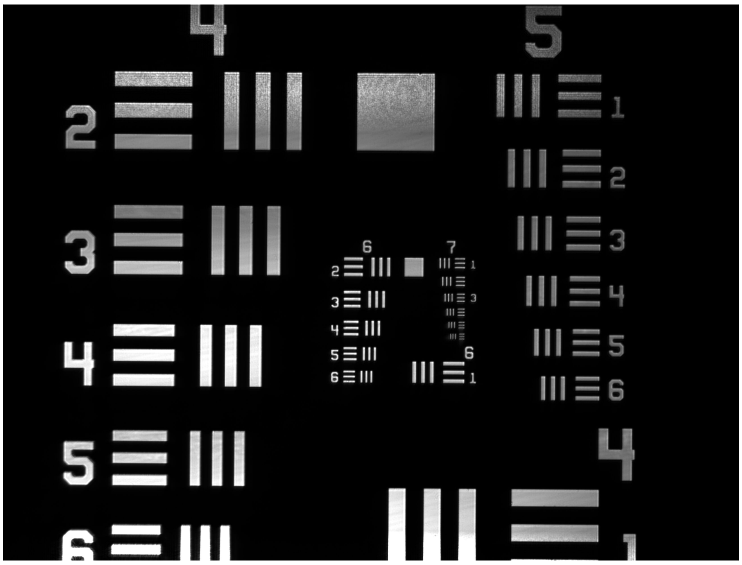

Figure 2.9: The best image acquired of the 1951 USAF resolution target. This image was used to determine the MTF of the objective with the viewport. The illumination is not perfectly uniform due to the finite refresh time of the camera and to the moving opaque tape. The sagittal lines correspond to the horizontal, the tangential the vertical, and only the data coming from group 6 and 7 is used to compute the MTF.

where $M(v)$ is the modulation of a pattern with spatial frequency v and $M(0)$ is the modulation of the overall background of the image (that can be considered in a good approximation equal to unity). From the simulation made with Zemax OpticStudio of the setup is possible to extract the diffraction-limited MTF.

The 1951 USAF test target (Figure 2.9) is used to measure experimentally the MTF curve. The target is placed on the focal point of the objective lens, that corresponds to the position where ions will be in the actual experiment. Ideally, one should use use an incoherent light source, and after filtering out the wavelength of interest implement the Köhler illumination method to evenly illuminate the target. In our case, laser light at 674 nm and a mobile piece of opaque tape have been used. A fast rotation of the tape immediately after the collimator causes the light to be scattered at different angles. After this, a $f = 25\,\mathrm{mm}$ aspherical lens collects the light coming from different directions to evenly illuminate the specimen from behind. A small pixel-size camera[12] is placed at the point where the image is expected to be formed after the objective lens. The final picture taken in this process is shown in Figure 2.9.

Even the smallest pattern in the target, 7th cluster in group seven (spatial frequency of 228.1 lines per mm) can be resolved with an acceptable contrast as reported in Figure 2.10. Eq. (2.6) is used to compute the values for the families in group six and seven the results are shown in Figure 2.10. From this, one can infere that our imaging system is almost diffraction limited. A contribution to the discrepancy is undoubtedly linked to the less than ideal illumination of the target. The illumination dis-uniformity can be noted in Figure 2.9 since a gradient of illumination from top to bottom is 'visible' in group four. This effect is less noticeable on groups with denser lines, as group six or seven, but still present. This is considered in the computation

---

[12] Allied Vision Alvium 1800 U-1240m, ($1.85\,\mu\mathrm{m} \times 1.85\,\mu\mathrm{m}$) pixel size.

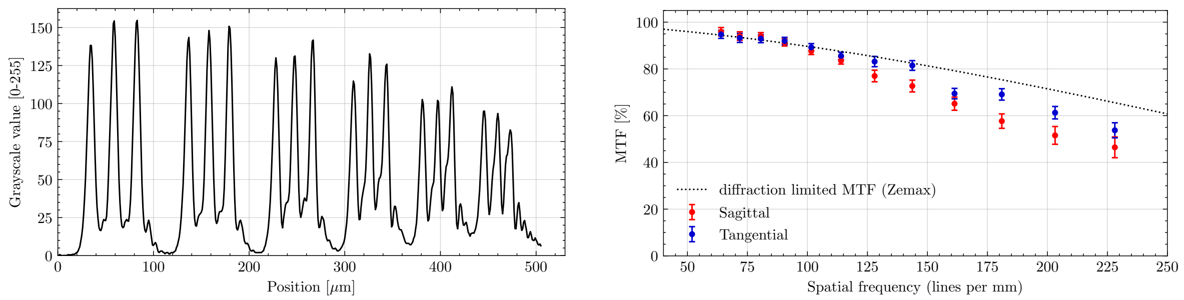

(a) Line graphs for group seven of Figure 2.9.

(b) MTF curve.

Figure 2.10: (a) Line graphs from group seven in the original greyscale image shown in Figure 2.9. One can easily spot the minima and the maxima of all the different six families, and also the smallest one can be clearly resolved. (b) Comparison between measurements and the simulation done with Zemax OpticStudio. Only the data coming from group six and seven are used to compute the MTF.

of the uncertainty associated to each measurement. In fact, the standard error for the peaks is the same for each group and takes the following form:

$$\sigma_{\text{peak}} = \sqrt{\frac{1}{N_f}\sum_f\sum_p\frac{(h_p - \langle h_p\rangle_f)^2}{N_p}}, \qquad \sigma_{\text{nadir}} = \sqrt{\frac{1}{N_f}\sum_f\sum_n\frac{(h_n - \langle h_n\rangle_f)^2}{N_n}}, \tag{2.7}$$

where $N_f = 6$ is the number of families in a group, h_p (h_n) is the height of a peak (nadir), and $\langle h_p\rangle_f$ ($\langle h_n\rangle_f$) is the average height of the peaks (nadirs) calculated on each family. For the final error on the MTF (Eq. (2.6)) the usual error propagation formula is used. As a final remark the fluorescence of the ions is not at 674 nm, but rather at 422 nm. Measurements were made at 674 nm as this was the only light available, but since good results are obtained in terms of resolution, a reduction in the wavelength can slightly improve them. Effects due to diffraction are in fact less present at smaller wavelengths.

Spot-size

To avoid cross-talking between nearest neighboring ions the spot size must be below 3 µm. Part of the characterisation involves an estimate of this quantity, which is given by taking into account the propagation law of a Gaussian beam reported in Eq. (2.10).

A small pixel-sized camera[13] is mounted on a unidirectional translation stage equipped with a micrometer screw, after the objective and roughly around its focal point (Figure 2.11, left). Right after the collimator, a neutral density filter and a gradient attenuator lower the laser power in order not to saturate the camera sensor. The camera is displaced with the micrometer screw along the optical axis and the gradient attenuator is rotated so as to get close to the point where pixels are saturated. Every 10 µm an image of the laser beam spot is saved. Each of them

---

[13] Allied Vision Alvium 1800 U-1240m, (1.85 µm × 1.85 µm) pixel size.

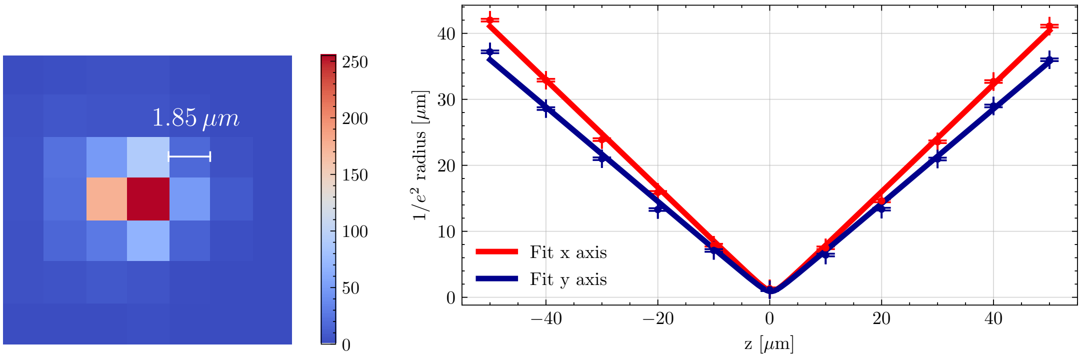

(a) Spot size close to the beam waist. Picture taken with the CMOS camera.

(b) Beam propagation

Figure 2.11: (a) The smallest measure of the beam size. Each square is a pixel of the CMOS sensor of the camera used during the characterisation. The spot size looks acceptable in terms of aberrations and a higher resolution camera could improve the measurement. (b) Gaussian beam propagation around the beam waist. The uncertainty on the x-axis is related to errors in the position measurement and follows a triangular distribution with $a = 1\,\mu\text{m}$ and the one on the y-axis is the result of the two-dimensional Gaussian fits at each position.

is being fitted with a two-dimensional elliptical Gaussian function of the form:

$$f(x, y) = A + B \cdot e^{-\frac{(x-x_0)^2}{2\sigma_x^2} - \frac{(y-y_0)^2}{2\sigma_y^2}}. \tag{2.8}$$

We do so in order to be able to detect any spherical aberration or astigmatism. The Gaussian beam radius in any position along the optical axis is given by the radial distance at which the intensity falls to $1/e^2 \cdot I_{\text{max}}$. From the two-dimensional Gaussian fit at each position z, the beam radius can be estimated as:

$$\omega(z) = \frac{\text{FWHM}(z)}{2\sqrt{2\ln 2}}. \tag{2.9}$$

From the theory of Gaussian optics, the beam radius propagates along the optical axis according to the following function:

$$w(z) = w_0\sqrt{1 + \left[\frac{(z - z_0)\lambda \text{M}^2}{\pi w_0^2}\right]^2}, \tag{2.10}$$

where z_0 indicates the waist position, i.e. the place where the beam radius has its minimum ω_0. M^2 is a dimensionless parameter known as the beam propagation ratio, and it gives an estimate of the discrepancy of the beam under examination from a Gaussian beam. Thus, we fit this function both for the x and y axes, obtaining the results summarized in Table 2.1. The spot sizes found are enough to reduce the cross-talking to the minimum.

2.4.3 AOD characterisation

The device used for deflecting the laser beam and address different ions in the 1D ion crystal is an acousto-optic deflector (AOD) [61]. A brief but comprehensive introduction to this device is now given. The operating principle is based on non-linear optical effects that arise when a crystal

	$2w_0$ [µm]	z_0 [µm]	M^2
$x-$axis	2.0(18)	0.4(3)	4(3)
$y-$axis	1.8(16)	0.2(4)	3(3)
Simulation	2.6	0	1

Table 2.1: Final measurements and simulated with Zemax OpticStudio. ω_0 is the waist radius, z_0 is the position of the waist and M^2 is the beam propagation factor. A value of M^2 close to unity indicates that the beam is similar to a Gaussian beam. However, higher values are obtained from the fit, but as can also be seen from Fig. the beam is astigmatic, i.e. it propagates differently along the two axes. This may be caused by the fact that the beam under investigation passes through a long optical setup and is the result of two first orders of diffraction. The measurements are compatible with the simulation result.

is excited by RF waves at frequency f_{RF} through a piezoelectric transducer. This oscillatory motion generates a refractive index wave in the crystal, which acts as a sinusoidal grating for the laser light passing through. In this way, the beam will be diffracted into several orders. The working principle of such acousto-optic devices can also be seen in the form of a 'precise collision' between the phonons of the RF acoustic wave and the photons of the laser beam passing through the crystal. For this reason, the output photon of the 1^{st} order of diffraction will have a different direction and a frequency shift of $\Delta f_{\mathrm{shift},1^{\mathrm{st}}} = f_{\mathrm{RF}}$. To do resonance operations on the ions, this shift can be compensated with one AOM placed upstream. In any case, the shifted beam can always be used to do off-resonant operations on the qubits. In our implementation, we place the 1^{st} order of diffraction on the optical axis and optimise for it in terms of diffraction efficiency (Section 2.4.3). The other orders are either blocked or have negligible intensities (less than 1 % with respect to 1^{st} order) or fall outside the addressing range. The angle of deflection of the first order depends on the applied frequency f_{RF}. The maximum achievable scan span angle of the first order of diffraction, depends on the bandwidth Δf_{RF}, on the speed of the acoustic wave v_a and on the wavelength λ used according to the law:

$$\theta_{\mathrm{scan},th} = \frac{\lambda(f_{\mathrm{RF},c} + \Delta f_{\mathrm{RF}})}{v_a} - \frac{\lambda(f_{\mathrm{RF},c} - \Delta f_{\mathrm{RF}})}{v_a} = \frac{\lambda \Delta f_{\mathrm{RF}}}{v_a}. \tag{2.11}$$

The AOD[14] implemented in our setup is a shear-mode on-axis deflector based on a $\mathrm{TeO_2}$ crystal, thus having an acoustic wave speed of $v_a = 617\,\mathrm{m\,s^{-1}}$. Its center frequency is $f_{\mathrm{RF},c} = 80\,\mathrm{MHz}$ with a bandwidth of $\Delta f_{\mathrm{RF}} = 40\,\mathrm{MHz}$ According to Eq. (2.11) then $\theta_{\mathrm{scan}} = 2.5°$ which is close to the one we measured of $\theta_{\mathrm{scan}} \approx 2.8°$. The type of crystal and the material employed are the main characteristics that give the AOD its deflection properties. As an example, the compensation AOM is also based on a $\mathrm{TeO_2}$ crystal, but put in a longitudinal mode. This means that $v_a = 4200\,\mathrm{m\,s^{-1}}$, and considering $\Delta f_{\mathrm{RF}} = 25\,\mathrm{MHz}$ the deflection angle is largely reduced. This is the substantial difference between an AOM and an AOD. On the other hand, a lower acoustic velocity results in a slower deflection of the beam itself as the acoustic wave takes longer to pass through the crystal.

For an incoming Gaussian beam, in the hypothesis that its divergence is much smaller compared to the one of the acoustic wave [61], the maximum number of resolvable angular positions

---

[14] ISOMET D55-T80S-2, $\lambda = 750\,\mathrm{nm} - 850\,\mathrm{nm}$, $f_{\mathrm{RF},c} = 80\,\mathrm{MHz}$, $\Delta f_{\mathrm{RF}} = 40\,\mathrm{MHz}$

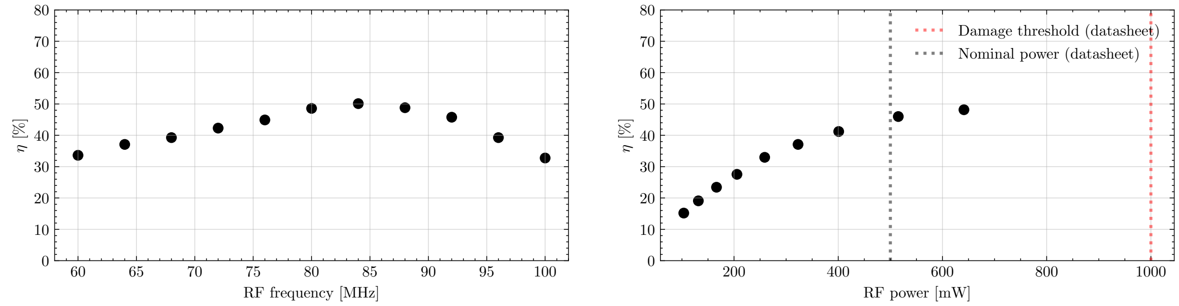

(a) η vs RF frequency at $P = 630\,\mathrm{mW}$.

(b) η vs RF at $f_{\mathrm{RF},c} = 80\,\mathrm{MHz}$.

Figure 2.12: Diffraction efficiency as a function of the applied RF frequency. The optimization was carried out so as to have more or less the same efficiency at the limits of the bandwidth.

can be determined as:

$$N = \Delta f_{\mathrm{RF}} \cdot \tau_{\mathrm{acc}}, \tag{2.12}$$

which is also known as the time-bandwidth product. In the last equation τ_{acc} is the access time, that in the datasheet is specified to be 11.3 µs. This time is the one required by the acoustic wave to pass the whole active aperture of the AOD (2 mm H × 7 mm L) at v_a. In the end, $N = 450$ spots can be resolved in principle by the deflector used. Eq. (2.12) is showing the trade-off between having a very fast deflector and one able to resolve a high number of angular positions. Details on how the AOD is powered with RF signals can be found in Section 2.4.3.

Diffraction efficiency

The diffraction efficiency is a crucial parameter for the power of the laser light reaching the ions. The most commonly way of defining diffraction efficiency consists of the ratio of the power in the first order of diffraction $P_{1^{st}}$ to the input power P_{in}:

$$\eta\,[\%] = \frac{P_{1^{st}}}{P_{in}} \cdot 100. \tag{2.13}$$

An ideal deflector should be able to guarantee the highest possible diffraction efficiency, constant over the entire frequency spectrum Δf_{RF}. To maximise η, the laser needs to enter the crystal at its Bragg angle:

$$\theta_{\mathrm{Bragg}} = \frac{\lambda f_{\mathrm{RF}}}{2 v_a}. \tag{2.14}$$

It should be noted that this is proportional to f_{RF}, and this results in a roll-off of diffraction efficiency as the frequency is varied. In our case, $\theta_{\mathrm{Bragg}} \approx 3°$ at $f_{\mathrm{RF},c}$, and the first thing that has been tried was to optimise η at this frequency. However, this results in an efficiency profile with a peak at the centre ($\eta \approx 55\,\%$) frequency and very low values ($\eta \approx 20\,\%$) at the extreme of the bandwidth. We therefore optimise the efficiency by having more or less the same value at the bandwidth limits but with an overall lower diffraction efficiency. The final measured profile is reported in Figure 2.12 (a).

The diffraction efficiency also depends on the RF power applied. The effect that can be seen is that diffraction efficiency increases with RF power, up to a point where it saturates. The final profile is reported in Figure 2.12. As specified by the manufacturer, the point at which the saturation starts is the nominal power ($P_n = 0.5\,\mathrm{mW}$), and when the power of 1 W is exceeded there is a potential risk of permanent damage to the crystal. After assembling the setup in the experiment and optimising the signal on the ions, the diffraction efficiency was measured again and noticeable changes were observed. η value has a rapid decrease (from $\approx 40\,\%$ to $\approx 20\,\%$) in the frequency range between $\approx 65\,\mathrm{MHz}$ and $\approx 73\,\mathrm{MHz}$. Even trying to re-optimise the efficiency of the AOD does not achieve the profile in Figure 2.12 (a). A way to overcome the problem, but which results in a lower diffraction efficiency (overall $\approx 20\,\%$) consists in driving the AOD with a power of 100 mW, far below nominal power.

Polarization requirements

During signal optimisation on ions, we ran into a problem related to signal stability. Whenever we changed the attenuation or frequency of the RF signal feeding the AOD, the population signal on the ion did not change abruptly. Rather, it fluctuated widely until it stabilised almost completely after a dozen seconds. By analyzing the polarisation of the light coming out of the AOD with a free-space polarimeter[15], we noticed how at each change of the AOD, the polarisation first jumped abruptly on the Poincaré sphere and then precessed on its surface. The characteristic times of the precession motion correspond approximately to the observed signal fluctuations. At this time the AOD was powered by a Direct Digital Synthesizers (DDS)[16], connected to the laboratory PC to run experimental sequences. It has been found that the Pulse box switches off all the DDS outputs each time a data point is collected. This introduces thermal fluctuations in the AOD that results in polarisation fluctuations on the beam directed towards the trap. To overcome this problem, we decided to install a TTL switch[17] that, as soon as the pulse box turns off its outputs, powers the AOD with a constant 80 MHz source[18] at the same RF power. In this way, the polarisation fluctuations are almost completely removed.

2.4.4 Characterisation of the addressing

With the apparatus mounted on an optical bench, it is possible to characterise the addressing range, and to study the feasibility of an input with a superposition of different RF signal at different frequencies. Similarly to how spot size was measured, we place the small pixel-sized camera[19] in the focus of the objective lens and measure the displacement of the beam along the axis of the chain from $f_{\mathrm{RF}} = 60\,\mathrm{MHz}$ to $f_{\mathrm{RF}} = 100\,\mathrm{MHz}$.

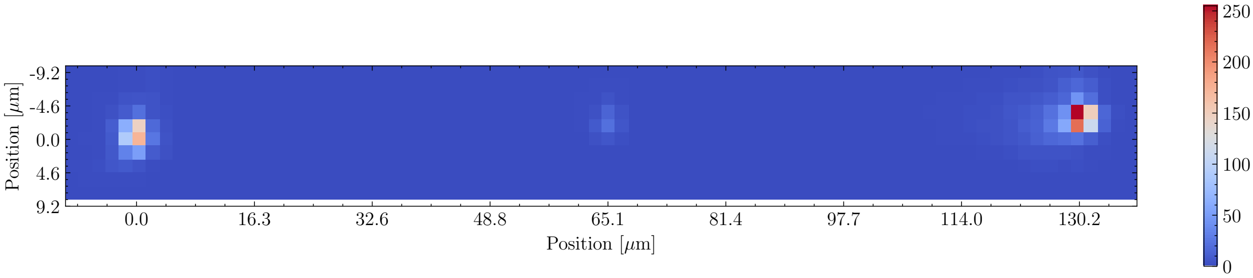

Figure 2.13: A portion of the CMOS camera sensor depicting 2 beam spots. An addressing range of 130 µm is measured by simultaneously powering the AOD with two frequencies: 60 MHz (left pixels excitation) and 100 MHz (right pixels excitation) corresponding to limits of the AOD frequency bandwidth. Additional excitations emerge due to non-linear effects in the AOD crystal and one of them is clearly visible in the centre.

Addressing range and multi-frequency input

The addressing range determines the number of ions that can be manipulated by the system. We use the Artiq "Phaser"[20] module instead of a normal DDS to carry out this measurement. This version with upconversion would in principle not allow RF signals to be used outside the window 300 MHz – 3.8 GHz but we have been able to lower the frequency window and thus cover the whole bandwidth of the AOD. Subsequently, a simple code was written to drive the oscillator in the first channel at 60 MHz and at 100 MHz simultaneously. In this way, the addressing range is measured with the camera and amounts to 130 µm (128 µm is the value obtained in the simulations described in Subsection 2.4.1). Considering numerical calculations for the spacing between ions [54] in a chain at an axial trapping frequency of $\omega_z = 2\pi \times 200\,\text{kHz}$ (achievable with a suitable combination of the end-cap electrodes voltage), it is in principle possible to control 30 ions individually. Further excitations emerge due to non-linear effects in the AOD crystal and one of them is clearly visible in Figure 2.13. In some quantum information processing contexts,

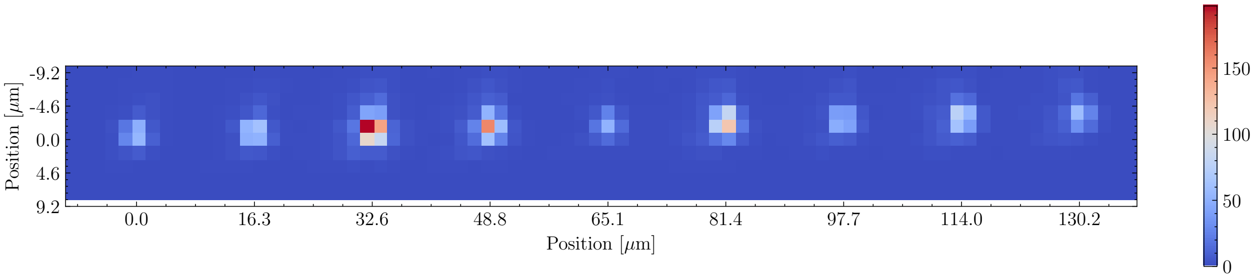

Figure 2.14: A portion of the CMOS camera sensor depicting 10 beam spots, generated by powering the AOD with ten different RF frequencies: from 60 MHz to 100 MHz in steps of 4 MHz.

---

[15] Thorlabs PAX1000VIS, 400 nm – 700 nm

[16] DDS5 from the Pulse box

[17] TTL signal corresponding to TTL30 on the Pulse box

[18] DDS11 from the Artiq box

[19] Allied Vision Alvium 1800 U-1240m, (1.85 µm × 1.85 µm) pixel size.

[20] The Phaser (with RF upconversion) is a FPGA-based dual channel Single Arbitrary Waveform Generator (SAWG) that allows us to work with 5 oscillators per channel.

it is also necessary to perform operations on several qubits simultaneously. With the ”Phaser” it is possible to use the 10 oscillators simultaneously and an example is shown in Figure 2.14. The output signals from the two channels is combined via a splitter[21] and then amplified in two stages[22,23]. The spot size is acceptable at each of the frequencies. Since this configuration will be used only in the future to address up to 10 ions, no further analysis was carried out. All the constraints imposed for this new single-ion addressing system are satisfied, and we are now ready to discuss results obtained by performing quantum operations on single ions.

---

[21] Mini-Circuits ZSFC-2-1-S+

[22] Mini-Circuits ZFL-500HLN+, +20 dB, +15 V DC

[23] Mini-Circuits ZHL-1-2W-S+,- +33 dB, +24 V DC

Chapter 3

Results

We are ready to work with a very precise sensor available in the laboratory: the strontium ion. In this chapter, some of the first results acquired with the single-ion addressing system are presented. In Section 2.4, it was described how the single-ion addressing setup has been designed and assembled. Subsequently, the setup has been characterised in order to be sure that all requirements are met. After this characterisation, the single-ion addressing system is ready to be installed on the actual trapped-ion experiment. The addressing optimisation procedure is explained in Section 3.1. Finally, it is shown in Section 3.2 how single-qubit off-resonant gates are performed on a three-ion chain.

3.1 Setup installation

The first step was to fix the breadboard in place and roughly centre the divergent beam with the radial viewport. Subsequently, the objective lens is installed and its position optimised in such a way that as little clipping as possible is observed on the output at the opposite side of the vacuum chamber. The output beam is a circle with a horizontal cut at both poles, due to clipping on the housing of the trap. By maximising the size and regularity of the circle exiting the trap, the focus of the Gaussian beam is placed close to the centre of the trap. From this point onwards, a single trapped ion and the PMT (Section 2.2) are used to optimise the addressing, starting with maximum power in the radial beam (by changing the attenuation in dB of AOM1 in Figure 2.2)). In addition to being able to select the intensity of the beam, the duration t of the pulses can be controlled. The ion is illuminated by pulsed light at 674 nm and if the beam is broad and not centred with respect to the ion position, quantum jumps can be observed. Initially, the main optical adjustment for the beam to perfectly hit the ion consists of moving the objective lens along the optical axis, i.e. back and forth with respect to the viewport. This also leads to a misalignment with respect to the imaging optics, which is then adjusted at a later stage. By moving the objective back and forth one can notice an increase in repetition rate of the quantum jumps, which in the end leads to a signal corresponding to a coherent excitation. Coherent excitation in turn corresponds to Rabi oscillations between the two levels, having a definite frequency Ω. Once small changes of the objective lens along the z axis result in large discrepancies in the signal, the two mirrors placed after the PBS (see Figure 2.7) are moved.

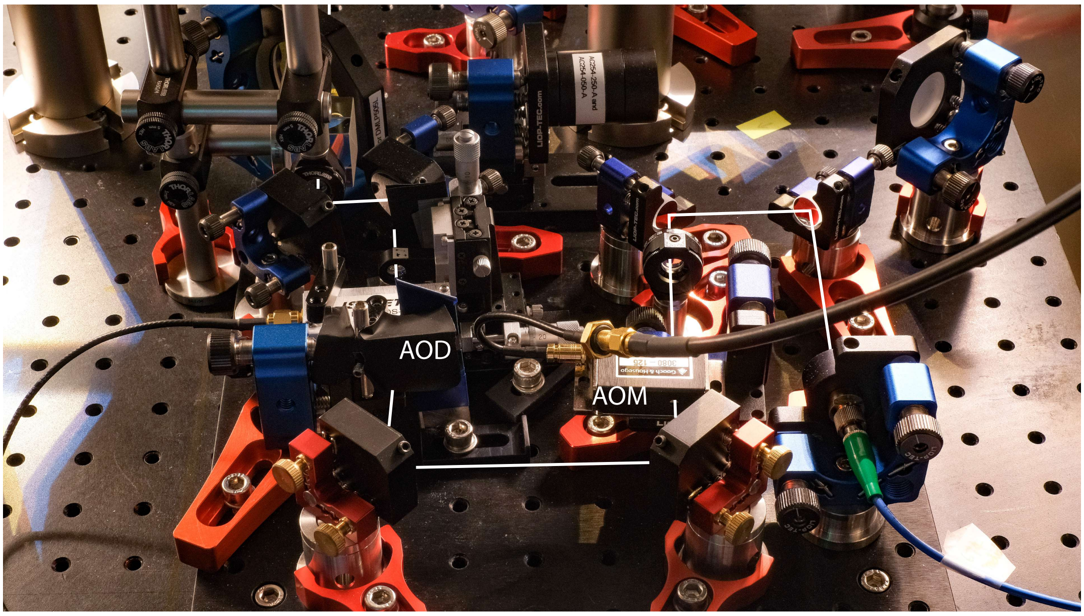

Figure 3.1: A picture of the final setup. All the optics are mounted on a breadboard so that it can be characterised on another optical table, and then mounted in the experiment when the characterisation is complete. The setup is compact in such a way that it also leaves room close by for the organization of other optical apparatus (such as single-ion addressing at Rydberg states). The white line indicates very roughly the path that light takes in the optical setup. Light enters via the collimator at the bottom right, continues by making a first U-turn and then enters the $\lambda/2$ plate and the first compensation AOM. The diffraction orders are reflected towards the AOD by other two mirrors, and both 0^{th} order and order $+2^{\text{nd}}$ are blocked by two blades mounted under the black aluminum foil (placed to avoid dangerous reflections outside the setup). The beam is diffracted again inside the AOD crystal and the 0^{th} order is blocked. The 1^{st} order is instead propagated through the $f = 16\,\text{mm}$ aspherical lens and in this way the beam is expanded to match the objective lens aperture (not in the picture).

The aim of this optimisation is to have a maximum excitation of the ion to the $|0\rangle$ ($4D_{5/2}$) level, as this corresponds exactly to a π flip in a time t. As soon as the signal is saturated for a certain laser beam power and a certain t, the intensity of the beam is attenuated and t is lowered. From a cruder point of view, we are looking for faster π flips with lower laser power. This is directly related to having a spot size better centred on the ion. The procedure is iterated until, following an attenuation of the laser beam or a decrease in t, the signal cannot be improved (i.e. no shorter π times can be reached with a maximum excitation to $|0\rangle$).

For finer adjustments it was also useful to move the ion along the trap axis, varying the voltage of one of the two end-cap electrodes and looking at the shape of the excitation (Figure 3.2). Thus, an ion is loaded in the trap and the potential of the right electrode (by looking at the trap from the direction where the radial beam is coming from) is varied in the range $1640\,\text{V} - 1780\,\text{V}$. The result of the ion excitation while passing through the beam focus is presented in Figure 3.2. As can be seen from Eq. (1.24) (setting $\Delta = 0$ for the resonant case), the resonance excitation is directly proportional to Ω^2, which in turn depends directly on the intensity $I \propto |\boldsymbol{E}_0|^2$ of the beam. The beam intensity in its focus should have a Gaussian profile. By following a procedure similar to that used in the estimation of the spot size with the camera (Section 2.4.2), we fit the

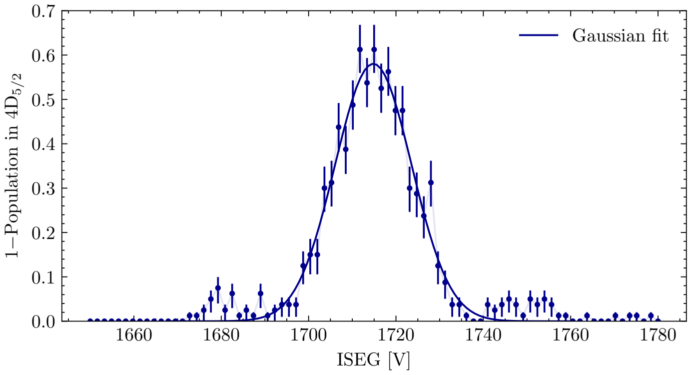

Figure 3.2: Scan of the endcaps trap potential. The voltage of the rightmost electrode (with respect to the direction the radial beam is reaching the trap) is varied in the range 1640 V – 1780 V. The pulse duration and power are optimised for the excitation not to saturate, as only in this case one can be sure that possible features in the profile are not related to saturation. The line connecting the points is placed to guide the eye in reading the graph.

data with a 1D Gaussian obtaining FWHM = 20.7(2) V. Taking into consideration the factor that converts a voltage displacement into a distance, estimated in Subsection 2.2.1, we obtain $2\omega_0 = 2.3(5)$ µm, a spot size compatible with the ones reported in Table 2.1. Symmetric features present on the left and right side of the central peak in Figure 3.2 are related to the first bright fringe of the Airy disc. Asymmetric components are instead related to optical aberrations.

3.2 Single qubit off-resonant gate

In this section we explain and demonstrate experimentally how to perform off-resonant gates on a qubit, exploiting the AC-Stark shift [62]. Both resonant and off-resonant laser pulses (with respect to the optical qubit transition) are needed to successfully perform these gates. We provide the former with the global axial beam, and the latter with the addressed radial beam. Considering a chain of ions, the procedure is the following:

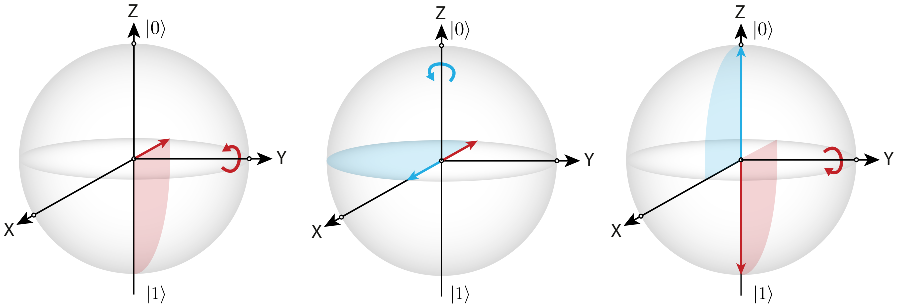

Figure 3.3: Off-resonant manipulation scheme. A first $\pi/2$ pulse with the resonant axial beam is performed on the ion chain. Then, with the off-resonant beam one or more ions are shifted in phase by $\phi = \pi$. As a last step, another $\pi/2$ pulse is carried out and the ions untouched by the off-resonant beam will go back to the initial state (red arrow). On the other hand, ions with the phase shifted by $\phi = \pi$ (blue arrow) will reach the other pole of the Bloch sphere.

- Ions are prepared in the state $|\psi\rangle = |1\rangle$ via optical pumping and a $\pi/2$ resonant global pulse with the axial beam for a duration of $t_1 = \pi/2 \cdot \Omega$ is performed. In this case the quantum states are moved from $|1\rangle$ to the equator of the Bloch sphere (left of Figure 3.3);

- With the tightly focussed laser beam from the radial direction, an off-resonant pulse is applied on the desired ion (or on multiple ions simultaneously) such that the AC-Stark shift rotates the qubit vector by $\phi = \pi$ on the equator. Since $\phi = \delta_{\mathrm{AC}} \cdot t_2$, the time t_2 (Ramsey time) must be properly optimized (centre of Figure 3.3) for a π shift;
- A final $\pi/2$ resonant global pulse with the axial beam for a duration of $t_3 = t_1$ is shone on the ions. The optical phase of this beam is shifted by π with respect to the one of the initial pulse. In this way, ions that were not hit by the off-resonant pulse return to $|1\rangle$, while those that underwent the π shift end up in $|0\rangle$.

The testing of this protocol and the characterisation of cross-talking are carried out on a three-ion chain. Thus, three ions are loaded into the trap to form a crystal. To ensure that the $\pi/2$ pulses interact equally along a string of ions, they are sent to the ions via the global beam installed along the axial axis. The axial laser beam frequency is optimised to be in resonance and the time for a π shift is measured to be $2t_1 = 70.40\,\mu\mathrm{s}$. Then, the radial beam is detuned by $\Delta = -8\,\mathrm{MHz}$ and centred with the central ion in the chain. The encoding of the optical qubit is done via Zeeman sub-levels, and since there are multiple of them, it is important to choose the Δ detuning accurately. In particular, the Δ value is chosen so that the coupling is out of resonance with the transition in the chosen Zeeman manifold, but still wanting this coupling to be the one that makes the greatest contribution to the oscillations. A closer study of the different transitions could lead to the choice of a different, more optimal detuning value. The time t_2 is optimised so that the phase shift in the central ion makes a π phase lap around the z axis: $t_2 = 40\,\mu\mathrm{s}$. As introduced in Subsection 2.4.3, each frequency shift in the AOD corresponds to a frequency shift in the laser light and thus to a further detuning from the electromagnetic transition. This shift is actively compensated for by varying the frequency of the AOM1 accordingly, to keep always a 8 MHz detuning. After optimising the signal for the central ion, an AOD frequency sweep is performed and the result is shown in Figure 3.4.

3.2.1 Cross-talk

$\varepsilon(1)$	$\varepsilon(2)$	$\varepsilon(3)$
2.9(1) %	3.0(1) %	3.1(1) %

Table 3.1: Addressing quality $\varepsilon(n)$ in a three ions chain, computed with Eq. (3.2). The Rabi frequencies used are those output from the fits of Eq. (3.2).

When carrying out quantum simulations or more general computation, it is important that the quantum states of individual ions can be manipulated without affecting those of their first neighbours. The largest contribution to this effect is caused by cross-talk between first neighbour ions. A smaller cross-talking corresponds to a better addressing quality. In turn, cross-talking may be due to a too large spot size of the focussed beam, or to optical aberrations causing

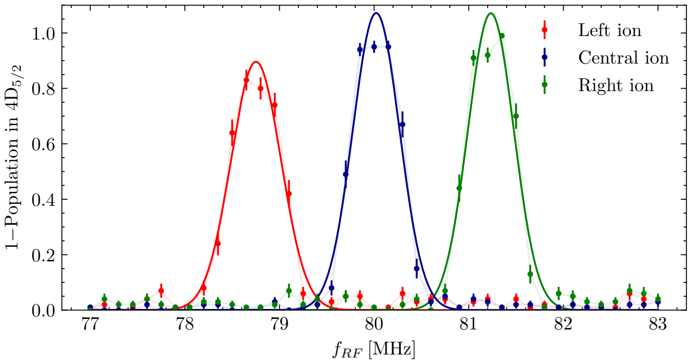

Figure 3.4: Frequency sweep of the AOD on a three ions chain. The position of the laser beam at 422 nm for fluorescence detection was not aligned with the centre of the trap, and this is the main reason why the peak on the left is lower than the others. The data shown were collected with the EMCCD camera. The difference in frequency between the peaks centers is 1.23 MHz. The line connecting the points is placed to guide the eye in reading the graph.

unwanted excitations on other ions. The figure of merit used to evaluate the addressing quality $\varepsilon(n)$ of ion n is the following:

$$\varepsilon(n)\,[\%] = \max\left(\frac{\Omega_{n\pm1}}{\Omega_n}\right)\cdot 100, \tag{3.1}$$

where Ω_i corresponds to the Rabi frequency measured for the i-th ion. Rabi oscillation measurements have the same π times of the resonant excitation optimised for the data obtained in Figure 3.4. The radial beam is deflected in such a way as to induce Rabi oscillations on each of the three ions individually. The time for a $\phi = \pi$ shift is optimised for the central ion and again amounts to $t_2 = 40\,\mu\text{s}$. The results of the Rabi oscillations for each of the three ions are shown in Figure 3.5. From the latter figure, an exponential damping of the oscillations can be seen and this is due to a non-optimal coherence time along the axial axis. One reason for this is that along the trap axis the ions are weakly confined and consequently the axial oscillation modes are populated by a higher number of phonons. A greater exchange of information with the environment therefore causes a decrease in the coherence time. For this reason, fits are not performed with the function introduced in Eq. (1.24), as the latter assumes a null number of phonons in the ion under consideration. A more suitable function to describe Rabi oscillations in general in the presence of a statistical mixture of states with different numbers of phonons was derived at p. 117 of [63], and reads as follows:

$$p_e(t) = \frac{1}{2}\left[1 - \frac{\cos(\Omega t) + (\Omega\langle\hat{N}\rangle\eta^2 t)\cos(\Omega t)}{1 + (\Omega\langle\hat{N}\rangle\eta^2 t)^2}\right], \tag{3.2}$$

where Ω is the Rabi frequency of the oscillations, $\langle\hat{N}\rangle$ is the expectation value of the number operator (number of phonons present in the system) and η is the Lamb-Dicke parameter (calculable via Equation 1.34). The parameter $\langle\hat{N}\rangle = 16$ is set in accordance with what is measured in [49] and what is expected in terms of the number of phonons from a string with only Doppler-cooled ions. A new measurement with relative error of the number of phonons would lead to a more

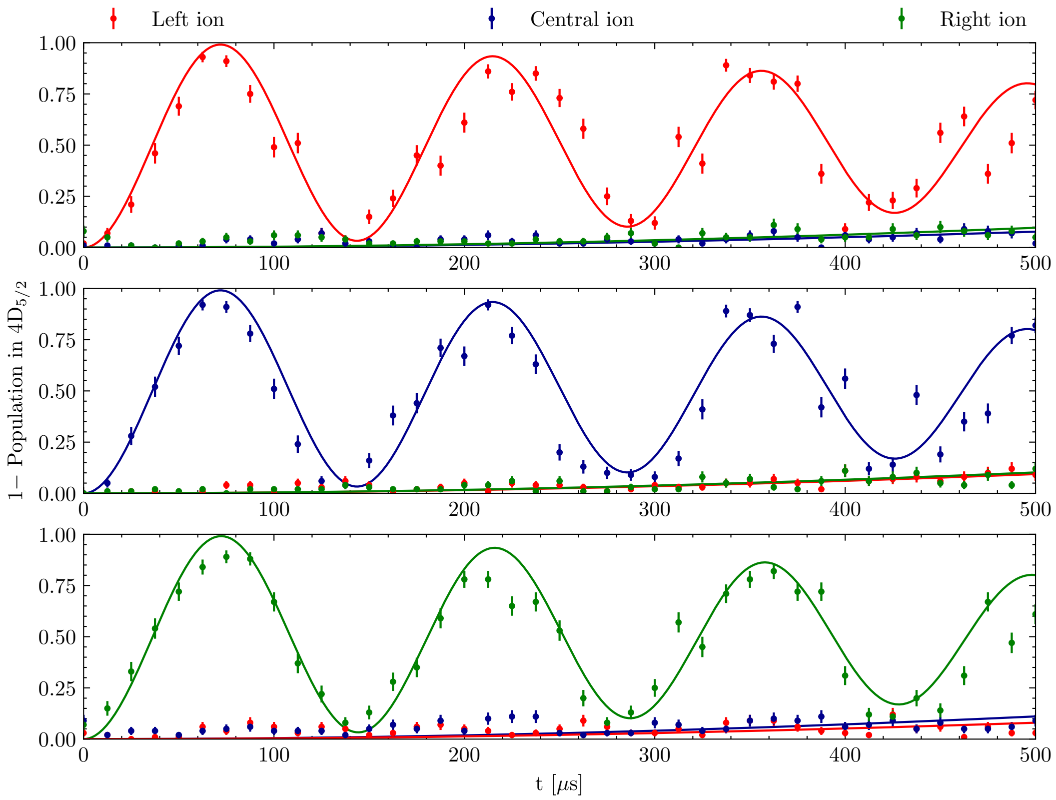

Figure 3.5: Rabi oscillations[1] for the central ion in a three ion chain. The protocol followed for these measurements is the one explained in Section 3.2. Briefly, the global axial beam is performing on each ion a $\pi/2$ pulse, and then a second $\pi/2$ pulse with an optical phase shift of π with respect to the first pulse. In between the two, the off-resonant radial beam induces an AC-Stark shift which corresponds to a π lap around the z axis. The ions that are being hit by the off-resonant light will reach $|0\rangle$ on the Bloch sphere, while the other goes back to $|1\rangle$ after the second $\pi/2$ pulse. Each point along the x-axis corresponds to a different duration of t_1 (and consequently t_3), i.e. a different application time of the $\pi/2$ pulse. The oscillations have two decaying exponential envelopes due to the sub-optimal coherence time along the axial axis. The type of pulses that are normally carried out in quantum computation are mainly π pulses or $\pi/2$-pulses, and these are guaranteed by the setup with minimal cross-talking (limited within three complete oscillations on each of the three ions). Error bars are calculated with the quantum error projection noise in Eq. (1.41) on a number of $N = 100$ measurements per point.

reliable estimate of the Rabi frequency of the oscillations and consequently to a better estimate of the addressing quality following Eq. (3.1). Instead, $\eta = 0.07$ is fixed to the value calculated with Eq. (1.34) for 674 nm, $\omega_z = 2\pi \times 1\,\text{MHz}$ of axial confinement and $\cos(\theta) = 1$ (the angle between the axial beam and the axial direction of motion is close to 0). By comparing the Rabi frequencies resulting from the fits and by using Eq. (3.1) we arrive at a final estimate of the addressing quality, reported in Table 3.1.

Summary and outlooks

The goal of this work was to have, within six months, a single-ion addressing system mounted in the trapped ions experiment at room temperature. This system should have been able to perform single-qubit gates in a chain of n ions. The first step was to get to grips with the Zemax OpticStudio software. A system capable of having a focused beam with a spot size smaller than 3 µm was simulated taking into account spatial constraints. The system should be also able to manipulate individually at least 10 ions in a string.

After working on the simulation, trying to comply with all the constraints imposed, the components of the setup were characterised precisely. In the first period, the objective lens was tested in terms of spot size, transmission efficiency and imaging capability. From this component, no irregularities were noted as focusing and imaging capabilities turned out to be as expected. This is a testament to the careful design of the objective lens on the part of Markus Hennrich. During the addressing calibration phase, the objective lens mount was modified to bring the last lens in the objective lens even closer to the viewport, thus moving the focus further inland and respecting the simulation distances. Prior to this project, the optical imaging system was not optimised and aberrations were clearly visible in the CCD camera image. This prevented three ions from being clearly distinguished. Some time was spent optimising this part of the experiment, simulating a section of it and considering different lenses. No further details are given as this is not the main topic of the thesis, but the result was a greater magnification and thus a better separation between neighbouring ions. The other fundamental component characterised was the AOD. The latter had been purchased before the start of the project, but due to shipping problems it arrived exactly halfway through the project. The obtained diffraction efficiency profile does not completely match the one specified in the datasheet, although a lot of time was spent on its optimisation. During the characterisation, the diffraction efficiency profile specified by the company is almost constant along the RF bandwidth, while the one measured drops slightly for frequencies close to the edges of the bandwidth.

The biggest challenge faced in this thesis project was the one related to thermal drifts of the AOD. As described in Section 2.4.3, during the signal optimisation process, it was noticed that the signal oscillated as a result of changes in the RF signal in the AOD. Further analysis led to the assumption that these were introduced by the Pulse box, in particular by the way it was delivering the RF signal. As soon as the way of supplying the RF signal was changed, using a constant signal from the Artiq box and an RF switch, the problem was curbed. Again by means of the Artiq box and the "Phaser" module, it was also possible to see how the deflector behaves when fed with a superposition of different RF signals at different frequencies. In the future, this could be used to do simultaneous single-ion addressing on 10 ions and carry out new quantum simulations.

In conclusion, the objective of this thesis project has been achieved. Some problems with the Pulse box put the characterisation for longer chains and two-qubit entanglement gates (Mølmer-Sørensen [31, 32]) on hold prematurely. The next steps, as soon as the problems are contained, will certainly involve a better characterisation of the single ion-addressing system on longer ion chains. New studies on how particular motional mode excitations propagate within the chain can also be carried out (on the same flow of ideas contained in this article [64]), or even study protocols of motion teleportation within the ion chain.

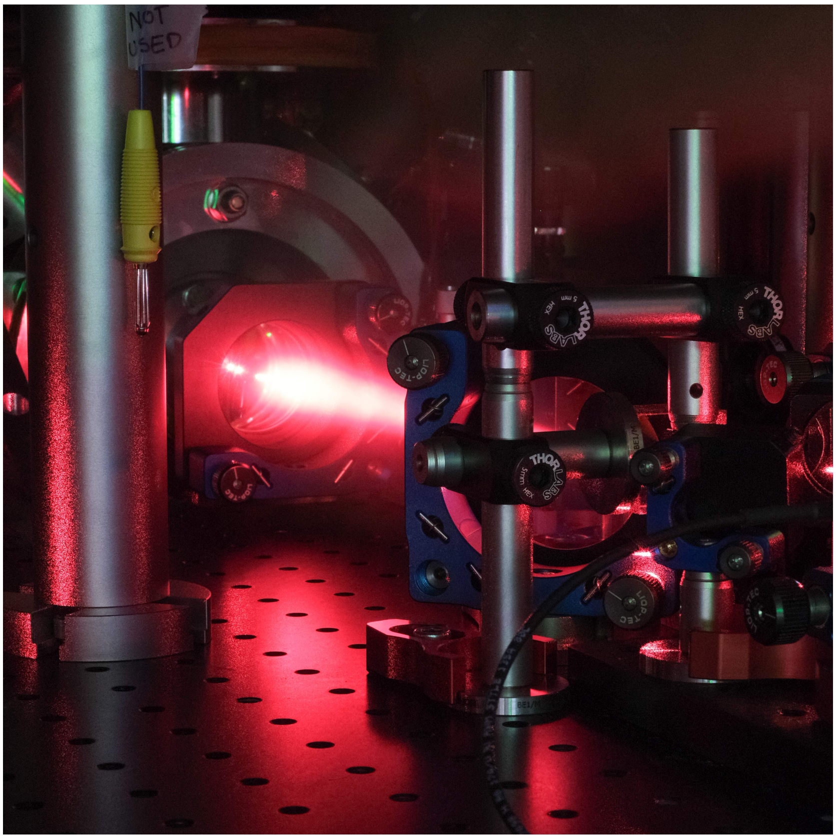

Figure 6: 40 seconds exposure in which the expanded beam at 674 nm can be seen.

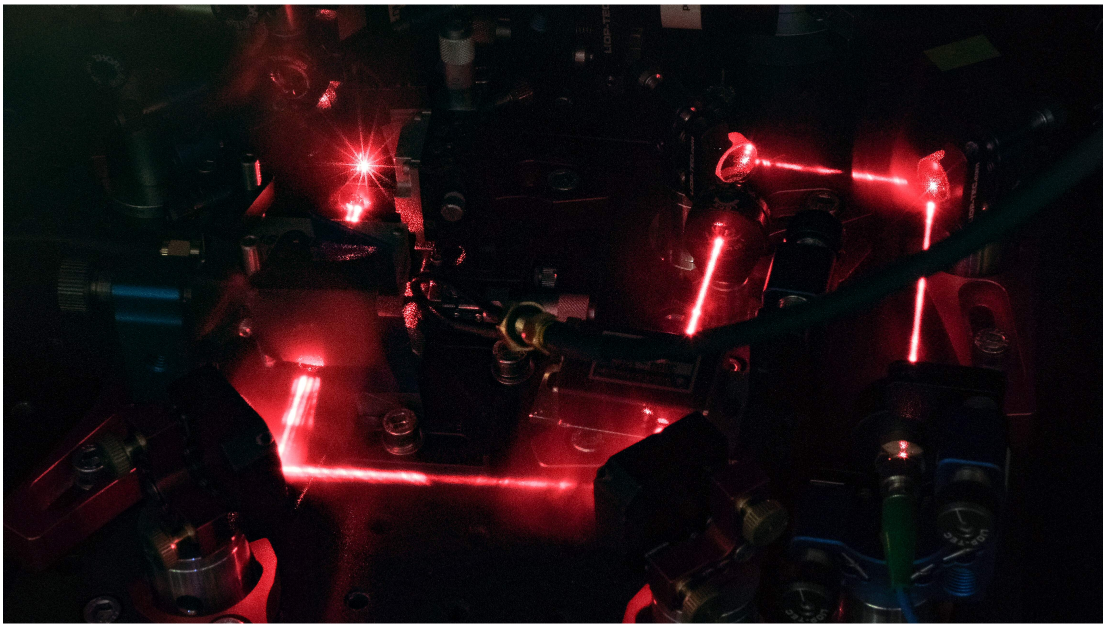

Figure 7: 40 seconds exposure of the entire setup. The diffraction orders of the AOM and of the AOD can be seen on the left. Both pictures are taken by opening the shutter for 40 seconds and moving a lens cleaning tissue along the beam path.

Acknowledgments

In these challenging years, and in the recent months in particular, I realised how interpersonal relationships are perhaps the only thing that really matters. This Master's thesis project, and more in general the six-months experience in Sweden, gave me a lot. First and foremost, I would like to thank my family, **Alessandro**, **Monica** and **Alberto** and my relatives, who always supported me during this experience. Next, I would like to thank **Elisabetta**, who is a very important person to me, and who has often visited me during this experience and has always managed to get me back on track, even in difficult times. A big thank you goes to my supervisor **Caterina Braggio**, who followed and always supported me from Padova during the work. Regarding the experience at Fysikum, I must thank my other supervisor **Markus Hennrich** for considering me and warmly welcoming me into the group, even though before this project I had little experience with laser physics and quantum optics. Whenever I needed to discuss something he was there, and with extreme calmness and clarity he always guided me towards the right choices. The person through whom I got to know better the reality in Stockholm and whom I trusted from the beginning was **Marion**, and I thank her very much for being there at the start, in the lab, and also during the correction of the thesis (I thank her even if she has been showing off the quantum hackathon T-shirt that I haven't received). I am also grateful to her for introducing me to her super flatmates, for sharing her private coffee beans and for making me feel welcome everywhere. I thank **Natalia** (my splendid office mate) and **Robin** for being there when we had to discuss optical designs, simulations and the functioning of the ARTIQ box. With them (and **Olek**, thank you!) I also went to beautiful concerts and walked through Tyresta National Park between frozen lakes and endless forests. Next, I would like to thank **Harry** for being with me to shoot some hoops and for giving me a lot of support in the final phase of optimising the apparatus built and measuring the first results with it. I also thank him for inviting me to play five-a-side football in Kappala and for not laughing at me given my clumsiness in that sport. I also am sure that you Harry will see where the problem lies in the experiment and that you can have coherence even outside the 9-minute window! Thanks also go to **André** (and **Lílian**!) and **Alan**, who make up the South American component of the group and who always listened and supported me in the more theoretical discussions. I also take this opportunity to thank **Shalina** and all the members of the other groups in the corridor, with whom we shared the lunch room and a few beers after work: **Thomas**, **Alban**, **Fernando**, **Zaxarias**, **Junior**, **Riccardo** and **Jaewon**. I was also very happy to meet **Sara** and **Luca**, two interns from the group, thanks to whom it was even more pleasant to go to the lab during the summer. Luca, I have to thank you for teaching me how to make proper carbonara! I link

to this to also thank all Marion's housemates at the house in Norrviken: **Thomas**, **Kiran**, **Vera**, **Kathinka** and **Afonso**. Thank you for all the wonderful dinners together, for the games of *The Fuzzies*, for *scarafaggio*, *stracciatella* and for all the days we climbed together. I know that in the future our lives will meet again and I can't wait! I thank my landlord **Mansour** for his warm welcome in the house in Stocksund and my flatmate **Tomasz** for making me laugh a lot, for being supportive and introducing me at best to the life in Sweden. I also thank all my wonderful friends from the climbing gym and in particular those with whom (unfortunately only at the end of my stay in Sweden) I went crag climbing and had a few beers! Lastly, I would like to thank my university friends in Padova from the bottom of my heart, on whom you can always count for anything: **Filippo**(s), **Christian**, **Samuele**, **Lorenzo**, **Alessandro**, **Giulia**, **Andrea**, **Sara**, **Giacomo** and **Cristina**.

Bibliography

[1] M. A. Nielsen and I. L. Chuang. *Quantum Computation and Quantum Information: 10th Anniversary Edition*. Cambridge University Press, (2010).

[2] R. P. Feynman. Simulating physics with computers. *International journal of theoretical physics*, **21**(6/7):467–488, (1982).

[3] E. Schrödinger. Are there quantum jumps ? *British Journal for the Philosophy of Science*, **3**(11):233–242, (1952).

[4] W. Paul and H. Steinwedel. Ein neues massenspektrometer ohne magnetfeld. *Zeitschrift Naturforschung Teil A*, **8**:448, (1953).

[5] I. Georgescu. Trapped ion quantum computing turns 25. *Nature Reviews Physics*, **2**:1–1, (2020).

[6] Y. Nakamura, A. Y. Pashkin, and J. S. Tsai. Coherent control of macroscopic quantum states in a single-Cooper-pair box. *Nature*, **398**, (1999).

[7] D. Loss and D. P. DiVincenzo. Quantum computation with quantum dots. *Physical Review A*, **57**:120–126, (1998).

[8] I. L. Chuang and Y. Yamamoto. Simple quantum computer. *Physical Review A*, **52**:3489–3496, (1995).

[9] D. Gottesman, A. Kitaev, and J. Preskill. Encoding a qubit in an oscillator. *Physical Review A*, **64**:012310, (2001).

[10] T. Ladd, F. Jelezko, R. Laflamme, Y. Nakamura, C. Monroe, and J. L. O'Brien. Quantum computers. *Nature*, **464**, (2010).

[11] Lov K. Grover. A fast quantum mechanical algorithm for database search. In *Proceedings of the twenty-eighth annual ACM symposium on Theory of computing - STOC '96*, pages (212–219), Philadelphia, Pennsylvania, United States, (1996). ACM Press.

[12] P. W. Shor. Polynomial-time algorithms for prime factorization and discrete logarithms on a quantum computer. *SIAM Journal on Computing*, **26**(5):1484–1509, (1997).

[13] T. Monz, D. Nigg, E. A. Martinez, M. F. Brandl, P. Schindler, R. Rines, S. X. Wang, I. L. Chuang, and Rainer Blatt. Realization of a scalable Shor algorithm. *Science*, **351**(6277):1068–1070, (2016).

[14] J. P. Buhler, H. W. Lenstra, and Carl Pomerance. Factoring integers with the number field sieve. In Arjen K. Lenstra and Hendrik W. Lenstra, editors, *The development of the number field sieve*, volume **1554**, pages 50–94. Berlin, Heidelberg, (1993). Series Title: Lecture Notes in Mathematics.

[15] J. I. Cirac. Quantum computing and simulation. *Nanophotonics*, **10**(1):453–456, (2021).

[16] I. M. Georgescu, S. Ashhab, and Franco Nori. Quantum simulation. *Reviews of Modern Physics*, **86**:153–185, (2014).

[17] A. J. Daley, I. Bloch, C. Kokail, S. Flannigan, N. Pearson, M. Troyer, and P. Zoller. Practical quantum advantage in quantum simulation. *Nature*, **607**, (2022).

[18] M. Rossmannek, P. Barkoutsos, P. J. Ollitrault, and I. Tavernelli. Quantum hf/dft-embedding algorithms for electronic structure calculations: Scaling up to complex molecular systems. *The Journal of Chemical Physics*, **154**(11):114105, (2021).

[19] A. Trabesinger. Quantum leaps, bit by bit. *Nature*, **543**, (2017).

[20] Arsuaga-Rios, M., Bahyl, V., Batalha, M., Caffy, C., Cano, E., Capitoni, N., Contescu, C., Davis, M., Fernandez A., D., Guenther, J., Karavakis, E., Keeble, O., Leduc, J., Luchetti, F., Mascetti, L., Murray, S., Patrascoiu, M., Peters, A., Kamil S., M., Sindrilaru, E., and Toebbicke, R. Lhc data storage: Preparing for the challenges of run-3. *European Physical Journal Web Conferences*, **251**:02023, (2021).

[21] D. DiVincenzo and IBM. The physical implementation of quantum computation. *Fortschritte der Physik*, **48**, (2000).

[22] I. Georgescu. The DiVincenzo criteria 20 years on. *Nature Reviews Physics*, **2**:1–1, (2022).

[23] V. Letchumanan, M. A. Wilson, P. Gill, and A. G. Sinclair. Lifetime measurement of the metastable $4d\,^2\mathrm{D}_{5/2}$ state in $^{88}\mathrm{Sr}^+$ using a single trapped ion. *Physical Review A*, **72**:012509, Jul (2005).

[24] H. C. Nägerl, Ch. Roos, D. Leibfried, H. Rohde, G. Thalhammer, J. Eschner, F. Schmidt-Kaler, and R. Blatt. Investigating a qubit candidate: Spectroscopy on the $S_{1/2}$ to $D_{5/2}$ transition of a trapped calcium ion in a linear paul trap. *Physical Review A*, **61**:023405, (2000).

[25] C. Monroe and J. Kim. Scaling the ion trap quantum processor. *Science*, **339**(6124):1164–1169, (2013).

[26] A. K. Ratcliffe, R. L. Taylor, J. J. Hope, and A. R. R. Carvalho. Scaling trapped ion quantum computers using fast gates and microtraps. *Physical Review Letters*, **120**:220501, (2018).

[27] J. Hilder, D. Pijn, O. Onishchenko, A. Stahl, M. Orth, B. Lekitsch, A. Rodriguez-Blanco, M. Müller, F. Schmidt-Kaler, and U. G. Poschinger. Fault-Tolerant Parity Readout on

a Shuttling-Based Trapped-Ion Quantum Computer. *Physical Review X*, **12**:011032, Feb (2022).

[28] P. Wang, C. Y. Luan, M. Qiao, M. Um, Z. Junhua, Y. Wang, X. Yuan, M. Gu, J. Zhang, and K. Kim. Single ion qubit with estimated coherence time exceeding one hour. *Nature Communications*, **12**, 01 (2021).

[29] D. Deutsch. Quantum computational networks. *Proceedings of the Royal Society of London. Series A, Mathematical and Physical Sciences*, **425**(1868):73–90, (1989).

[30] F. Schmidt-Kaler, H. Haeffner, M. Riebe, S. Gulde, G. Lancaster, T. Deuschle, C. Becher, C. Roos, J. Eschner, and R. Blatt. Realization of the Cirac-Zoller controlled-NOT quantum gate. *Nature*, **422**:408–11, 04 (2003).

[31] A. Sørensen and K. Mølmer. Quantum computation with ions in thermal motion. *Physical Review Letters*, **82**:1971–1974, (1999).

[32] K. Mølmer and A. Sørensen. Multiparticle entanglement of hot trapped ions. *Physical Review Letters*, **82**:1835–1838, (1999).

[33] J. Preskill. Quantum Computing in the NISQ era and beyond. *Quantum*, **2**:79, August (2018).

[34] W. Paul. Electromagnetic traps for charged and neutral particles. *Reviews of Modern Physics*, **62**:531–540, (1990).

[35] L. S. Brown and G. Gabrielse. Geonium theory: Physics of a single electron or ion in a Penning trap. *Reviews of Modern Physics*, **58**:233–311, (1986).

[36] D. Leibfried, R. Blatt, C. Monroe, and D. Wineland. Quantum dynamics of single trapped ions. *Reviews of Modern Physics*, **75**:281–324, (2003).

[37] F. Pokorny. Experimental setup for trapping strontium rydberg ions. Master dissertation, Innsbruck University, (2014).

[38] A. Pöschl. Laser ablation loading and single ion addressing of strontium in a linear paul trap. Master dissertation, KTH Stockholm, (2018).

[39] H. Parke. *Applications of motional control in trapped Rydberg ion experiments.* Licentiate thesis, Stockholm University, (2022).

[40] F. Pokorny. *A microwave dressed Rydberg ion.* PhD dissertation, Stockholm University, (2020).

[41] E. Mathieu. Mémoire sur le mouvement vibratoire d'une membrane de forme elliptique. *Journal de Mathématiques Pures et Appliquées*, **13**:137–203, (1868).

[42] M. Drewsen and A. Brøner. Harmonic linear paul trap: Stability diagram and effective potentials. *Physical Review A*, **62**:045401, (2000).

[43] M. Brownnutt. *$^{88}Sr^{+}$ ion trapping techniques and technologies for quantum information processing.* PhD dissertation, Imperial College London, (2007).

[44] E. Biemont, J. Lidberg, S. Mannervik, L.O. Norlin, P. Royen, W. Shi, A. Schmitt, and X. Tordoir. Lifetimes of metastable states in sr ii. *The European Physical Journal D - Atomic, Molecular, Optical and Plasma Physics*, **11**(3):355–365, (2000).

[45] F. Schmidt-Kaler, T. Feldker, D. Kolbe, J. Walz, M. Müller, P. Zoller, W. Li, and I. Lesanovsky. Rydberg excitation of trapped cold ions: a detailed case study. *New Journal of Physics*, **13**(7):075014, (2011).

[46] A. Lindberg. Improving the coherent quantum control of trapped ion qubits. Master dissertation, Stockholm University, (2020).

[47] P. Barakhshan, A. Marrs, A. Bhosale, B. Arora, R. Eigenmann, and M. S. Safronova. Portal for High-Precision Atomic Data and Computation (version 2.0). University of Delaware, Newark, DE, USA.

[48] H. Zhang, M. Gutierrez, G. H. Low, R. Rines, J. Stuart, T. Wu, and I. Chuang. Iterative precision measurement of branching ratios applied to $^{88}\mathrm{Sr}^{+}$. *New Journal of Physics*, **18**(12):123021, (2016).

[49] G. Higgins. *A single trapped Rydberg ion.* PhD dissertation, Stockholm University, (2018).

[50] D. F. V. James. Quantum dynamics of cold trapped ions with application to quantum computation. *Applied Physics B*, **66**(2):181–190, (1998).

[51] R. Loudon. *The Quantum Theory of Light. Third Edition.* Oxford University Press, (2000).

[52] R Blatt, G Lafyatis, W D Phillips, S Stenholm, and D J Wineland. Cooling in traps. *Physica Scripta*, **T22**:216–223, (1988).

[53] M. Ringbauer, M. Meth, L. Postler, R. Stricker, R. Blatt, P. Schindler, and T. Monz. A universal qudit quantum processor with trapped ions. *Nature Physics*, (2022).

[54] T. P. Meyrath and D. F.V. James. Theoretical and numerical studies of the positions of cold trapped ions. *Physics Letters A*, **240**(1):37–42, (1998).

[55] A. H. Burrell, D. J. Szwer, S. C. Webster, and D. M. Lucas. Scalable simultaneous multi-qubit readout with 99.99% single-shot fidelity. *Physical Review A*, **81**:040302, (2010).

[56] C.S. Adams and E. Riis. Laser cooling and trapping of neutral atoms. *Progress in Quantum Electronics*, **21**(1):1–79, (1997).

[57] D.J. Wineland and H. Dehmelt. Proposed $10^{14}\delta\nu < \nu$ laser fluorescence spectroscopy on TI^{+} mono-ion oscillator II (spontaneous quantum jumps). *Bulletin*, **20**:637, (1975).

[58] S. Stenholm. The semiclassical theory of laser cooling. *Reviews of Modern Physics*, **58**:699–739, (1986).

[59] E. Abbe. Beiträge zur theorie des mikroskops und der mikroskopischen wahrnehmung. *Archiv für mikroskopische Anatomie*, **9**:413–418, (1873).

[60] W.J. Smith. *Modern Optical Engineering, 4th Ed.* McGraw Hill professional. McGraw-Hill Education, (2007).

[61] I.C. Chang. I. Acoustooptic Devices and Applications. *IEEE Transactions on Sonics and Ultrasonics*, **23**(1):2–21, (1976).

[62] H. Häffner, S. Gulde, M. Riebe, G. Lancaster, C. Becher, J. Eschner, F. Schmidt-Kaler, and R. Blatt. Precision measurement and compensation of optical stark shifts for an ion-trap quantum processor. *Physical Review Letters*, **90**:143602, (2003).

[63] C. Roos. *Controlling the quantum state of trapped ions.* PhD dissertation, Innsbruck University, (2000).

[64] M. Tamura, T. Mukaiyama, and K. Toyoda. Quantum walks of a phonon in trapped ions. *Physical Review Letters*, **124**:200501, (2020).